Towards Development of an Empirical Model for Prediction of Screech and Coupling in Supersonic Rectangular Twin Jets

Undergraduate Honors Thesis

Presented in Partial Fulfillment of the Requirements for Graduation with Honors Research Distinction in the Department of Mechanical and Aerospace Engineering at The Ohio State University

By

Samuel Yoder

The Ohio State University

2022

Thesis Committee

Prof. Mo Samimy, Advisor

Dr. Nathan Webb

Abstract

Rectangular twin jet engines used on tactical aircraft have several advantages compared to circular twin jet engines, namely, reducing an aircraft's weight and drag, improving its maneuverability, and integration of propulsion and aerodynamics. However, relatively little research has been done on the flow and acoustic characteristics of rectangular twin jet engines. Coupling between the two jets due to their close proximity introduces unsteady pressure fluctuations in the near field and noise in the far field which, if not controlled, can cause high levels of sonic fatigue as well as intense radiated noise. This can damage critical components close to the nozzles and is a health concern for those nearby. This project will investigate the use of Localized Arc Filament Plasma Actuators (LAFPAs). LAFPAs, controlled electronically, create plasma arcs at the nozzle lip, producing thermal perturbations with desired frequencies in the flow which interrupt the predominant mechanism of jet noise, screech. Additionally, LAFPAs can alter the coupling behavior of the jets. However, due to the complex nature of the flow, it is difficult to predict the behavior of the jets to excitation by LAFPAs. As such, a physics-based empirical model has been developed to predict the response of the flow to certain actuation parameters. To accurately model this response, two important parameters must be determined: the locations of shock cells within the flow and the velocity of the large-scale flow structures convecting downstream within the jet, interacting with the shock waves, and generating screech tones. In this research, a method for empirically predicting streamwise shock locations based solely on flow Mach number is developed. Additionally, a novel method of estimating convective velocity is presented using Empirical Mode Decomposition (EMD) to isolate the hydrodynamic pressure from the measured overall (acoustic and hydrodynamic) pressure just outside the jets.

Acknowledgments

I would like to thank my advisor, Dr. Mo Samimy, for his careful guidance throughout this process and for being a great teacher. I would also like to thank *soon-to-be* Dr. Ata Esfahani for his thoughtful help through the duration of the project and for his endless patience. Thank you also to Dr. Nathan Webb who made a very difficult subject matter extremely approachable. Thanks also to Ryan Leahy for his contributions to experimental setup and recommendations. Finally, thank you to the Ohio Space Grant Consortium for their generosity and support.

Table of Contents

List of Tables

List of Figures

Nomenclature

c	Ambient speed of sound [m/s]
D_e	Equivalent nozzle diameter [m]
f_{crit}	Critical frequency [Hz]
L_n	Nondimensional shock cell location [m]
M_d	Nozzle design Mach number [-]
M_j	Flow Mach number [-]
U_c	Convective velocity [m/s]
U_j	Flow velocity [m/s]
$\tau_{c,i}$	Screech feedback loop period for reference jet [s]
$\tau_{s,i}$	Screech feedback loop period for secondary jet [s]
s	Nozzle center-to-center spacing [m]
α	Shock spacing coefficient [-]
κ	Initial shock location coefficient [-]
ϕ	Coupling phase angle [rad]

Chapter 1: Introduction

1.1 Jet Noise

The advent of the turbojet engine forever changed the world, allowing us to fly further and faster than propellor-driven aircraft ever could; however, there is a drawback to this performance – noise. The roaring low-frequency drone of jet-powered aircraft flying overhead is considered routine today, but efforts to reduce the noise generated by jet engines have been underway since their adoption. NASA began exploring methods to address jet noise as early as 1945, soon after the first turbojets began flying [1]. The simplest way to reduce jet noise is to reduce the exit velocity of the jet – for low supersonic Mach numbers, sound power levels scale with exit velocity by a power of six [2]! In high-bypass ratio turbofans, the large engines mostly used on commercial airliners, a reduced exit velocity has the added benefit of increasing overall efficiency. Noise generated by high-bypass ratio turbofans has steadily decreased over time due to incremental efficiency improvements, stricter FAA regulations, and the advancement of noise reduction technologies such as chevrons (See Figure 1.1) [3]. However, in tactical aircraft such as fighter jets, which have extremely high specific thrust demand, these large fan diameters are impractical. To compensate, they use smaller low-bypass turbofans with much faster exit velocities which are much noisier. Jet noise is more than just an annoyance, it can have serious long-term consequences for both people working near these aircraft *and* on the aircraft structure itself.

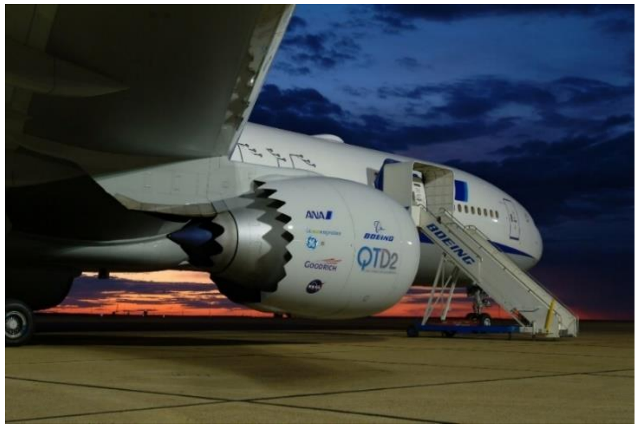

Figure 1.1: Chevrons on the nozzle of a GE90 mounted on a Boeing 777 [4]

Due to the complex nature of jet noise, little research has been done on less traditional jet configurations such as jets with non-axisymmetric nozzles [5]. The Gas Dynamics and Turbulence Laboratory (GDTL) at The Ohio State University has done extensive work in jet noise reduction with a focus on active control methods. One method explored is the use of Localized Arc Filament Plasma Actuators (LAFPAs) to control supersonic flows at various operating regimes. LAFPAs produce periodic thermal perturbations at the nozzle lip which alter jet behavior. In previous work at the GDTL, LAFPAs have been used with single and twin axisymmetric jet configurations. This work focuses on their use with closely-spaced, rectangular twin jets.

1.1.1 Supersonic Jet Flow

Many jet engines exhaust flow in the supersonic regime. That is, flow which is travelling at faster than the ambient speed of sound. To accelerate a compressible fluid such as air to supersonic speeds from subsonic ($M_j < 1$) speeds, flow must pass through a converging-diverging (C-D) nozzle. Due to a large pressure difference between the upstream of the nozzle and the ambient surroundings air, flow is accelerated through converging section of the nozzle until it reaches Mach 1 at the nozzle's smallest cross-sectional area, also known as the throat. After this point in the nozzle, the flow accelerates further as it expands through the remainder of the nozzle. For any given C-D nozzle there is a design Mach number (M_d) at which the flow is ideally expanded. This design Mach number is solely a function of the ratio between the nozzle's throat and exit areas.

When flow is exhausting from a C-D nozzle at a pressure ratio other than the design condition shock waves can be generated at the nozzle exit. For the purposes of this work, it is necessary to understand both the overexpanded (Mach number less than the design Mach number) and underexpanded (Mach number higher than the design Mach number) flow regimes. In overexpanded the pressure ratio between the nozzle exit and ambient air is lower than the design pressure ratio. Overexpanded flow will exhaust from the nozzle at the design Mach number but at a static pressure lower than the ambient air. Due to this pressure difference, the flow turns in on itself producing an oblique shock which is shown in Figure 1.2.

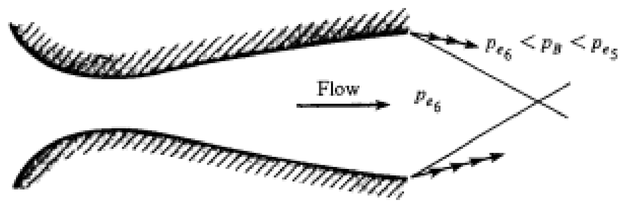

Figure 1.2: Diagram showing overexpanded flow exiting a converging-diverging nozzle [6]

In underexpanded flows, the ratio between the pressure at the nozzle exit and the ambient air pressure is greater than the design pressure ratio. Similarly, the flow will exhaust from the nozzle exit at the design Mach number but conversely the flow at the nozzle exit has a higher static pressure than the ambient air. As such, the flow expands outward in an expansion fan in order to equilibrate the pressure; it accelerates as it is expanded. This phenomenon is shown in Figure 1.3.

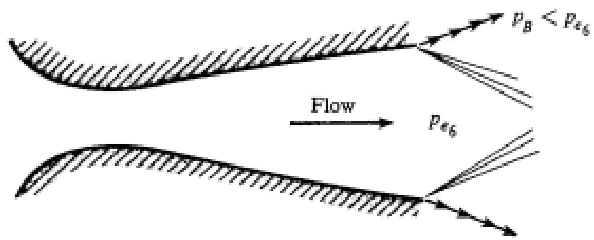

Figure 1.3: Diagram showing underexpanded flow exiting a converging-diverging nozzle [6]

It is important to understand both of these off-design flow regimes because aircraft cannot always, and rarely do, exhaust ideally expanded flow from their engines. Several factors affect ambient static pressure such as altitude and weather patterns and although some tactical aircraft are equipped with variable geometry nozzles, they cannot always compensate for outside factors.

As noted, in both off-design regimes there exist some kind of shock system after the nozzle exit which equilibrate the static pressure of the flow to the static pressure of the ambient air.

Figure 1.4: J-58 turbojet test fire with full afterburner showing shock diamonds [7]

In supersonic jet flows, this shock system, a series of shocks, continue to form downstream of the nozzle exit in a pattern known as shock diamonds which is shown in Figure 1.4. Expansion fans and oblique shocks in the jet plume extend outward until they reach to sonic line within the jet shear boundary where they are then reflected back inward. This process continues downstream until the shock system is dissipated by viscous forces. This train of reflecting shocks is known as the jet core and it decreases in size as the flow moves downstream. The area surrounding the jet column where the ambient and supersonic air interact is called the mixing layer. These components are labeled in Figure 1.5.

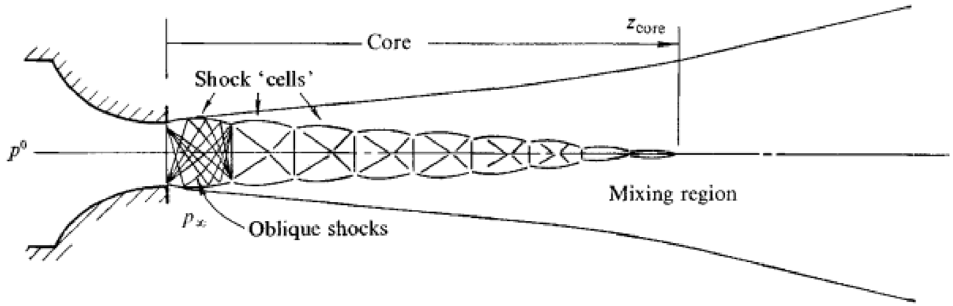

Figure 1.5: Diagram showing moderately underexpanded flow ejecting from a converging nozzle [8]

1.1.2 Components of Jet Noise

Jet noise can be split into two categories: mixing noise and Shock Associated Noise (SAN). The latter can be further divided into Broadband Shock Associated Noise (BBSAN) and screech. Mixing noise is generated dominantly by large-scale turbulent structures (LSSs) convecting downstream in the jet. A small portion of mixing noise is also due to fine-scale structures as well [9]. Turbulent structures result from small perturbations in the mixing layer near the nozzle lip which cause the fast moving jet flow to mix with the ambient surroundings. The large velocity gradient between the jet and its surroundings causes the flow to form vortices which become larger as they convect downstream [10].

In a single axisymmetric supersonic jet, mixing noise intensity is highest in the downstream direction and often occupies the lower frequency portion of the jet noise spectrum. The mixing noise intensity and directivity are dependent on jet Mach number and the ratio of jet and ambient temperature [9].

BBSAN is unique to supersonic jets because it is caused by the interactions of shock within the flow with the ambient air. Specifically, BBSAN is generated by large scale turbulent structures interacting with the shock cells in the jet core. When LSSs pass over a shock cell it generates an acoustic wave and is perceived as noise. Screech is a special case of SAN which occurs when this same mechanism creates a self-perpetuating feedback loop. The flow at the nozzle lip is particularly sensitive to perturbations due to its high energy density, so when the acoustic wave reaches the lip it creates an instability wave which travels downstream until it interacts with a shock cell and the process is repeated. This generates a discrete tonal noise, the fundamental screech frequency, followed by a series of harmonics whose frequencies are integer multiples of the fundamental frequency. Figure 1.6 shows a typical jet noise spectrum.

This phenomenon was discovered by Powell in 1951 who, using a homemade Schlieren imagery setup, was able to photograph this effect [10]. Since then, many researchers have made efforts to predict screech frequency.

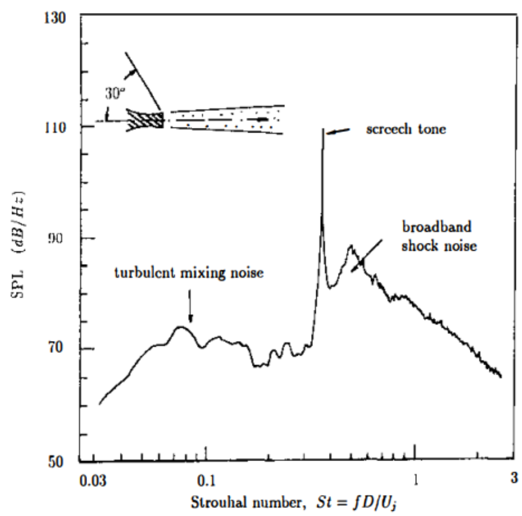

Figure 1.6: Typical supersonic jet noise spectrum from underexpanded axisymmetric jet with microphone at 30° with respect to the nozzle streamwise axis [11]

1.1.3 Consequences

Numerous studies have shown that long-term exposure to aircraft noise increases risk for health issues such as cardiovascular disease and hypertension even for those who just live *near* an airport [12], [13]. These issues are even more concerning for those who work near aircraft on a daily basis, such as military personnel on aircraft carriers. The nearly constant exposure to noise with little recovery time can lead to permanent hearing loss even if crew wear protective equipment [14]. Jet noise can also damage components on the aircraft itself.

In tactical aircraft such as fighter jets, the engine nozzle exits are often near critical control surfaces such as the F-22 shown in Figure 1.7. This introduces rapid pressure fluctuations which can fatigue nearby components over time. With the extensive use of composites and costly stealth coatings in newer aircraft this issue is becoming increasingly relevant [15]. Many fighter jets use a twin jet configuration in which two engines are mounted very close to one another (such as the F-22) which can be desirable for jet performance. However, coupling between the two jets due to their proximity can introduce much stronger pressure fluctuations in the near field compared to a single jet. Because of this, sonic fatigue is of particular interest for twin jet configurations, especially due to the complex mechanical components near and around the nozzles which are necessary to meet the high performance requirements of next generation tactical aircraft [16].

Figure 1.7: F-22 Raptor with afterburners on [17]

1.2 Rectangular Twin jet Configuration

Rectangular twin jets have multiple advantages compared to more conventional axisymmetric configurations which address rising performance demands for next-generation aircraft. Their shape allows for smoother integration into the body of the aircraft and therefore less drag and weight [18]. Additionally, the two-dimensional nozzle geometry allows for simpler thrust vectoring implementation as well as thrust reversal. These benefits poise rectangular twin jets as an attractive option for new aircraft so it is essential to better understand the flow characteristics of this configuration.

Recent work in the GDTL has explored the coupling modes of rectangular twin jets [5]. Jets in this configuration couple in both in-phase or out-of-phase flapping modes. When the jets are coupled in-phase, wavefronts reach both nozzle lips simultaneously. These wavefronts do not necessarily originate from the same jet – due to their spacing. Coupling behavior changes with M_j [19]. After extensive work at the GDTL, it has been shown that the jets primarily couple out-of-phase in the underexpanded regime and in-phase in the overexpanded regime. Around the design Mach number, flow transitions from out-of-phase to in-phase.

1.3 Empirical Screech Closure Model

The purpose of this thesis is to aid the development of an empirical method to predict screech and coupling behavior in a supersonic rectangular twin jets configuration. The basis for the method was developed by Dr. Nathan Webb, a research scientist at the GDTL. It is based on interactions between turbulent structures and shocks in the flow. Accurate predictions of jet behavior require estimates of both shock cell locations and convective velocity; methods for estimating both parameters are explored in this work.

1.3.1 Motivation

Predicting screech and coupling in supersonic jets has long been a topic of interest. Previous research has developed methods of predicting frequencies at which screech *could* occur for given conditions [20]. However, at this time, few works investigate the prediction of an exact screech frequency and its harmonics. Given the importance of screech and coupling phenomena, a method of accurately predicting jet behavior would be extremely beneficial in developing active jet flow and acoustic control methods. In the GDTL, this model will inform actuation parameters for LAFPAs to be used with supersonic rectangular twin jets.

1.3.2 Governing Principles

The basis for this model relies on the interactions between large-scale structures and shock tips downstream of the nozzle lip. The time required to complete one screech feedback cycle to shock tip i is given by the Equation 1 below and is governed by the convective velocity of the LSS (U_c) and the ambient speed of sound (c) where $L_{s,i}$ is the distance of shock tip i from the nozzle lip.

$$\tau_{s,i} = L_{s,i}\left(\frac{1}{U_c} + \frac{1}{c}\right) \tag{1}$$

Similarly, in order to model the interactions with the second nozzle in twin jets a slightly modified equation is used that accounts for the extra distance the acoustic waves travel where s is the spacing between the two nozzles' centerlines.

$$\tau_{c,i} = \left(\frac{L_{s,i}}{U_c} + \frac{\sqrt{L_{s,i}^2 + s^2}}{c}\right) \tag{2}$$

Supposing the LSS are generated at a particular frequency (f), and that the acoustic feedback waves are sinusoidal. The interference pattern $W(t)$ of the feedback waves from both jets at the nozzle lip can be written as the following equation.

$$W(t) = \sum_{i=m}^{n} \cos\left(2\pi f(t - \tau_{s,i})\right) + \sum_{i=m}^{n} \cos\left(2\pi f\left(t - \tau_{c,i}\right) + \phi\right) \tag{3}$$

Where ϕ describes the coupling mode between the two jets (in-phase: $\phi = 0$, out-of-phase: $\phi = \pi$). Also, where m and n are respectively the upstream-most and downstream-most shock tip interactions of interest. Typical values are 2 and 5 for m and n respectively. It was assumed that structures upstream of the 2nd shock cells would not be sufficiently developed for LSS/shock tip interaction to occur. Additionally, it was assumed that downstream of the 5th shock cells the structures would have disintegrated or would be too weak to interact in a meaningful way. Evaluating Equation 3 at $t = 0$ yields the amplitude of the perturbation which reinforces the feedback loop at a given frequency and flow conditions. This is hereafter referred to as the "perturbation amplitude." The perturbation amplitude can be calculated for both in-phase and out-of-phase conditions over a range of frequencies for a given flow condition. Sample results for the $M_j = 1.50$ case are shown in Figure 1.8.

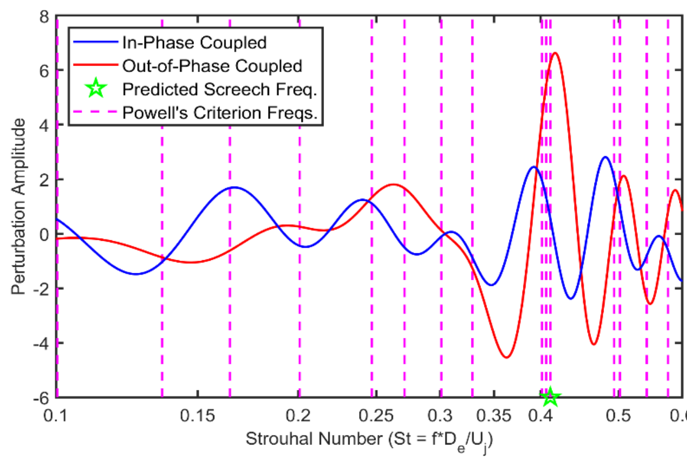

Figure 1.8: Sample screech closure model perturbation amplitude plot for $M_j = 1.5$

Note, the magenta dashed lines represent frequencies that satisfy "Powell's timing criterion", essentially frequencies at which the feedback loop has the potential to be self-sustaining [21]. The blue and red lines respectively represent the perturbation amplitude for in-phase and out-of-phase coupling modes. For the purposes of this work, it is enough to say that higher perturbation amplitudes indicate stronger feedback waves, and therefore the jet will eventually screech at the frequency with the highest perturbation amplitude. The exact screech frequency is then assumed to be the largest perturbation amplitude at which Powell's timing criterion is satisfied.

In summary, the model requires the following parameters: the ambient speed of sound, the convective velocity of the LSS, and the distance of the 2nd-5th shock tips from the nozzle lip. The sound speed is trivially calculated using the temperature from a thermocouple in the testing chamber, but the other two parameters need to be determined. This is the focus of this research.

1.3.3 Localized Arc Filament Plasma Actuators (LAFPAs)

LAFPAs are novel active flow control devices developed by the GDTL. Fundamentally, they work by introducing large thermal perturbations into a flow which have the potential to disrupt natural flow structures. LAFPAs were not specifically used for this work but their potential to control coupling and screech in the configuration analyzed is well documented [5]. The output of the screech closure model will provide insight into LAFPA excitation parameters which will alter desired flow characteristics.

Chapter 2: Experimental Methodology

2.1 Anechoic Chamber

All experimental testing was done at the GDTL at Ohio State's Aerospace Research Center (ARC). Compressed air is stored in a series of high pressure tanks with a capacity of 43 m^3 and maximum pressure of 16 MPa. The air is dried, filtered, and fed to the jet plenum. The pressure in the plenum is maintained by a computer-controlled valve in order to achieve the desired exit Mach number. Air from the plenum is then exhausted horizontally through the nozzle assembly, into an anechoic chamber. This air exits via a collector opposite of the nozzle where it is directed outdoors. If necessary, the flow can be heated up to a stagnation temperature of 500 °C; this was not used for this study. Additionally, forward flight conditions can be simulated at airspeeds up to 100 m/s through a co-flow duct that surrounds the nozzle assembly. This duct was not used for this work and was covered in acoustic foam to prevent reflections.

A schematic of the anechoic chamber is shown in Figure 2.1. It measures 6.2 *m* x 5.6 *m* x 3.4 *m* and has a cut-off frequency of 160 Hz (the lowest frequency which the sound proofing is effective). This cut-off frequency is well above those of interest in this research. Figure 2.2 shows a panoramic view of the chamber. Further details on the chamber are given by Hahn [22].

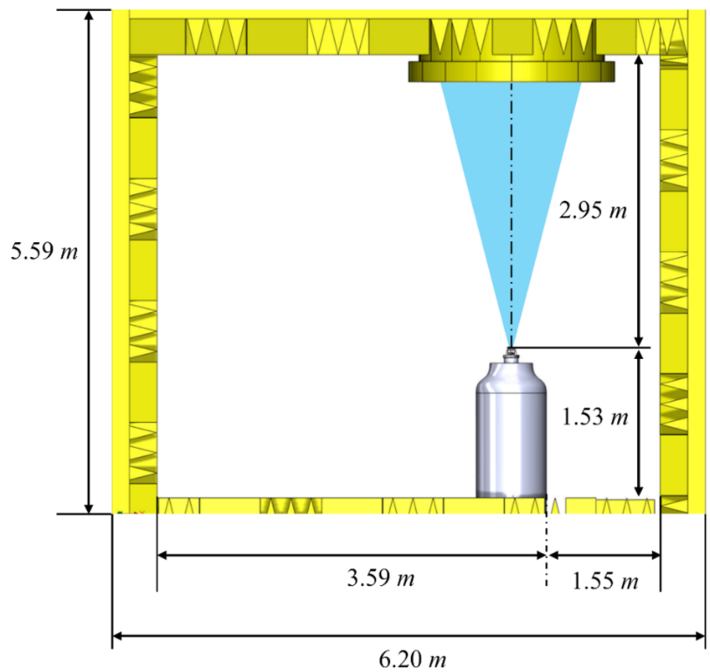

Figure 2.1: Schematic of the GDTL's anechoic chamber

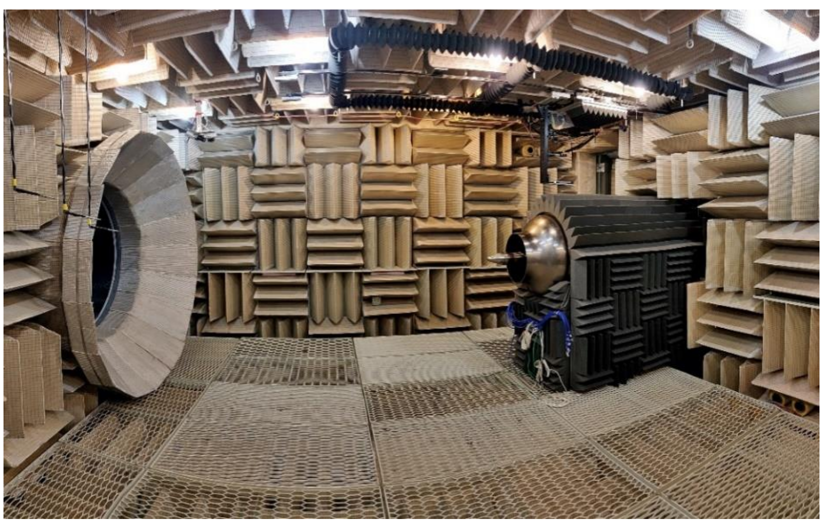

Figure 2.2: Panoramic view of anechoic chamber showing nozzle assembly (right) and collector (left)

2.2 Nozzles

The rectangular twin jet nozzle assembly was designed and built by the GDTL with modularity in mind. The nozzle assembly consist of two sharp-throated converging-diverging nozzles with a design Mach number (M_d) of 1.50. A dimensioned section view and isometric view are shown in Figure 2.3. The nozzles in the current configuration have an aspect ratio (AR) of 2 with width and height of 24.13 mm and 19.25 mm respectively. The nozzles have an equivalent area-based diameter (D_e) of 19.25 mm. That is, what the diameter of the nozzles would be if they were axisymmetric at the same exit area. The center-to-center spacing between the jets is 43.38 mm which is equivalent to $2.25D_e$.

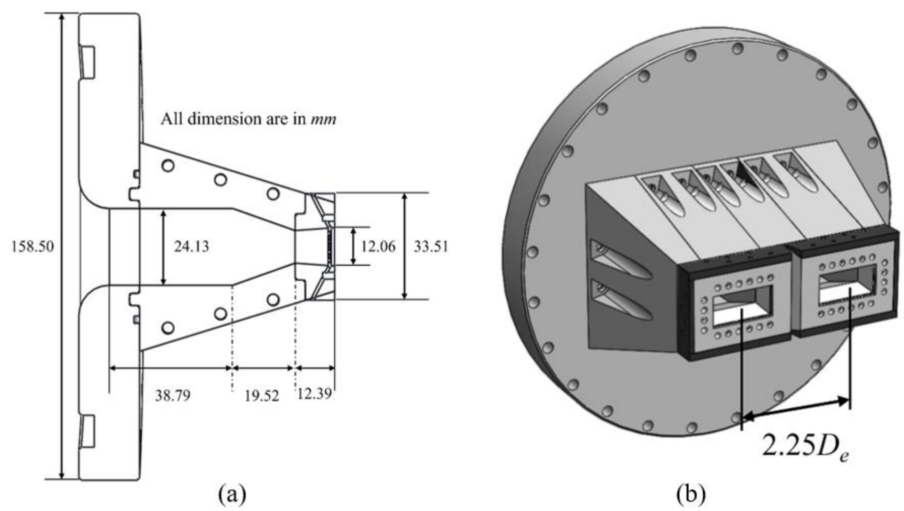

Figure 2.3: a) Dimensioned section view of nozzle showing sharp throat; b) twin jet assembly showing nozzle spacing

The nozzle assembly is fastened to the end of a pressurized air pipe and is sealed with a custom metal O-ring. Figure 2.4 shows the nozzle installed in the co-flow channel. After the assembly's installation, a thorough campaign was performed to verify the ideally expanded Mach number. Far-field microphone data was analyzed over a range of Mach numbers from 1.40 to 1.60 in increments of 0.05. The ideally expanded Mach number was inferred based on the spectra (specifically the screech amplitude and BBSAN peaks). Note, that due to the sharp throat design, shocks are still present in the jet when ideally expanded. It was found that the ideally expanded Mach number was very near $M_d = M_j = 1.50$.

Figure 2.4: Nozzle assembly installed in co-flow chamber

The LAFPA housings are made of boron nitride to prevent arcing to metal components. There is a 1 mm wide by 0.5 mm deep groove in the actuator block where the tungsten electrode tips sit, approximately 1 mm upstream from the nozzle lip. Previous testing at the GDTL has established that this groove does not affect the control authority of the LAFPAs [23]. The tungsten electrode tips sit flush with the inner nozzle wall, and there are set screw holes located around the perimeter of the nozzle lip. Figure 2.5 shows cross sections of both the nozzle assembly and an actuator block.

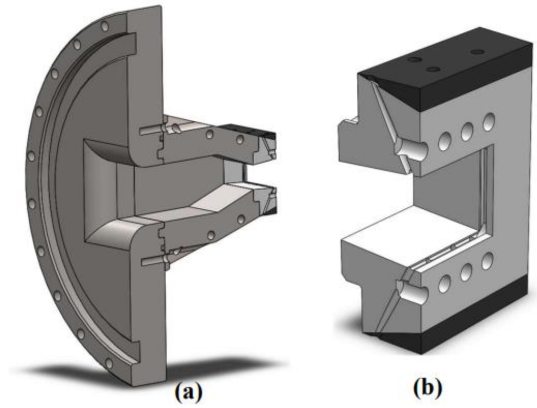

Figure 2.5: a) Cross-section of nozzle assembly; b) cross-section of actuator block

2.3 Linear Microphone Array

A linear array of 10 Brüel & Kjær 4939 ¼ in. microphones (with grid caps installed) was used to measure convective velocity. They have a relatively flat frequency response up to approximately 80 kHz and a dynamic range of 28 to 164 dB with a sensitivity of 4 mV/Pa. The microphones were secured using a ceiling-mounted stand which was covered in acoustic foam to prevent reflections. The microphones were set in two separate configurations over the centerline of the right jet (looking upstream) with the first optimized for the overexpanded regime ($M_j = 1.20 - 1.50$) and the second for the underexpanded regime ($M_j = 1.60 - 1.90$). Figure 2.7 shows the two configurations and the mount. The locations of the microphones in these configurations were optimized to best capture the shock cells for the given flow regime. Ryan Leahy, a graduate student at the GDTL, determined these best locations by analyzing shock locations in instantaneous schlieren images at various flow Mach numbers (see Figure 2.6). It was determined for both arrays that an angle of 10° relative to the horizontal was best in order to keep the microphones close to but outside the jet mixing layer. Initial microphone locations for configurations 1 and 2 respectively are as follows: $\left({}^{x}/_{h} = 1.1, {}^{y}/_{h} = 1.89\right)$ and $\left({}^{x}/_{h} = 4.2, {}^{y}/_{h} = 2.24\right)$.

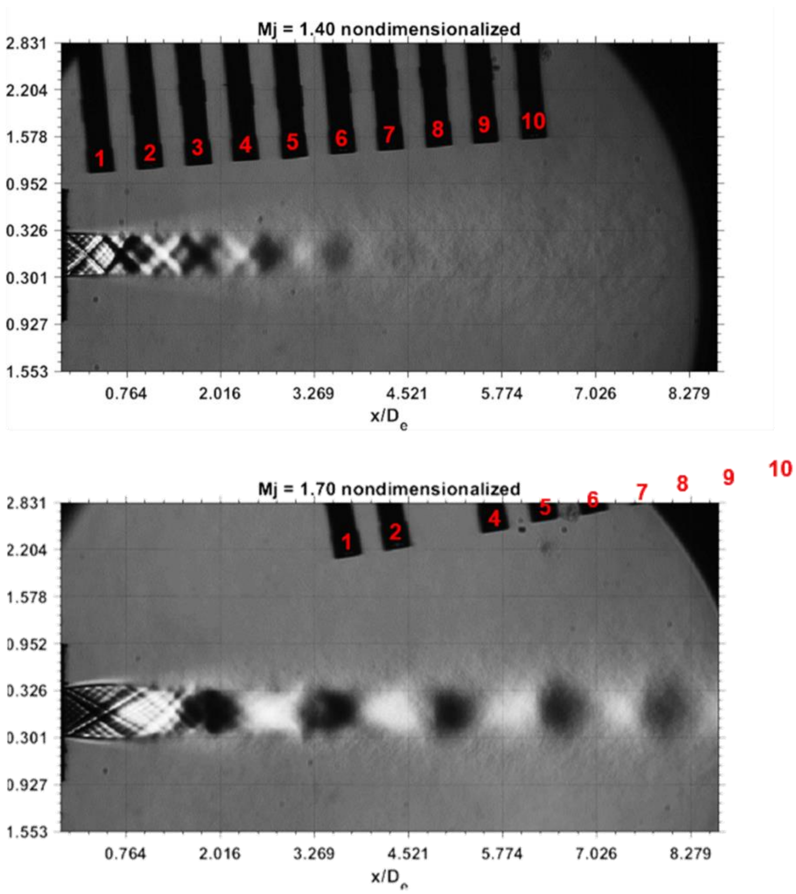

Figure 2.6: Schlieren images showing two linear near field microphone configurations

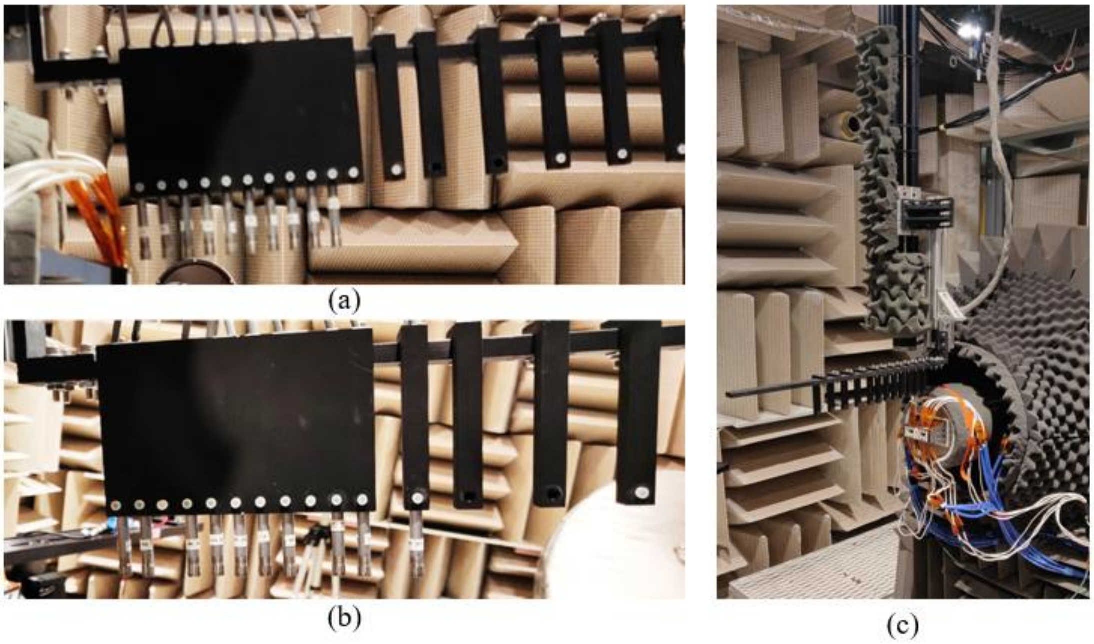

Figure 2.7: a) Config. 1 for overexpanded regime; b) Config. 2 for underexpanded regime; c) Linear microphone mount

2.4 Time-Averaged Schlieren Imaging

Time-averaged schlieren images were collected using a standard Z-type schlieren system with a LaVision Imager cCMOS camera with a 5.5 MP sensor. The knife edge was oriented vertically to highlight horizontal density gradients. For each M_j, 300 images were captured at 50 frames per second at a resolution of 2500 x 2150 pixels. Light was provided by a HPLS-36 high-powered pulsed LED from Lightspeed Technologies with a pulse width of 500 *ns*. This pulse width is narrow enough to showcase even the highest frequency screech tones. Figure 2.8 shows a panoramic view of the schlieren setup.

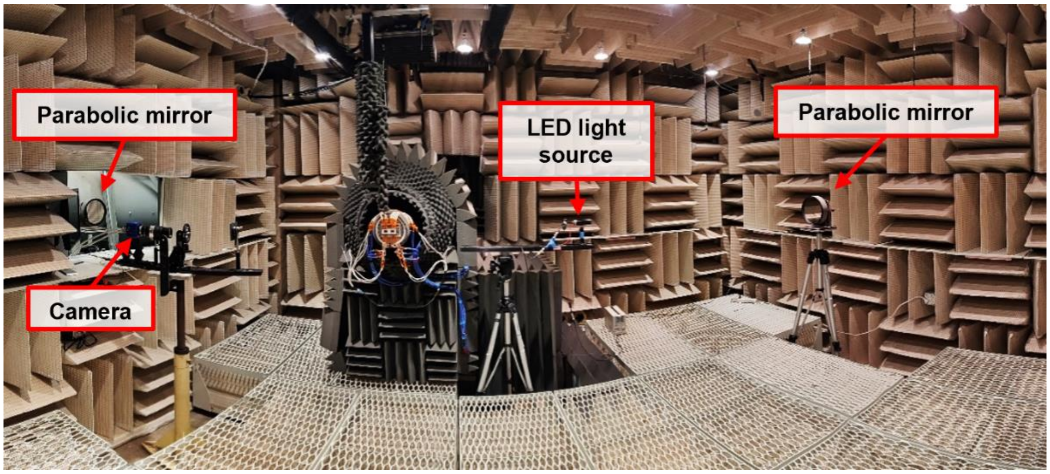

Figure 2.8: Schlieren imaging setup

2.5 Data Acquisition

Signals collected by the near field linear microphone array were amplified and filtered via a band-pass between 20 Hz and 100 kHz using Brüel & Kjær 2690 Nexus conditioning amplifiers. Microphone gain values were set using a Brüel & Kjær calibrator (model 4231). For each M_j tested, 100 blocks were collected at 32,768 samples per block and a sampling rate of 200 kHz. The signal was recorded with a National Instruments PXI-6133 A/D board and LabVIEW software. Figure 2.9 shows a schematic of the DAQ including a thermocouple near the nozzle exit and equipment for the LAFPAs.

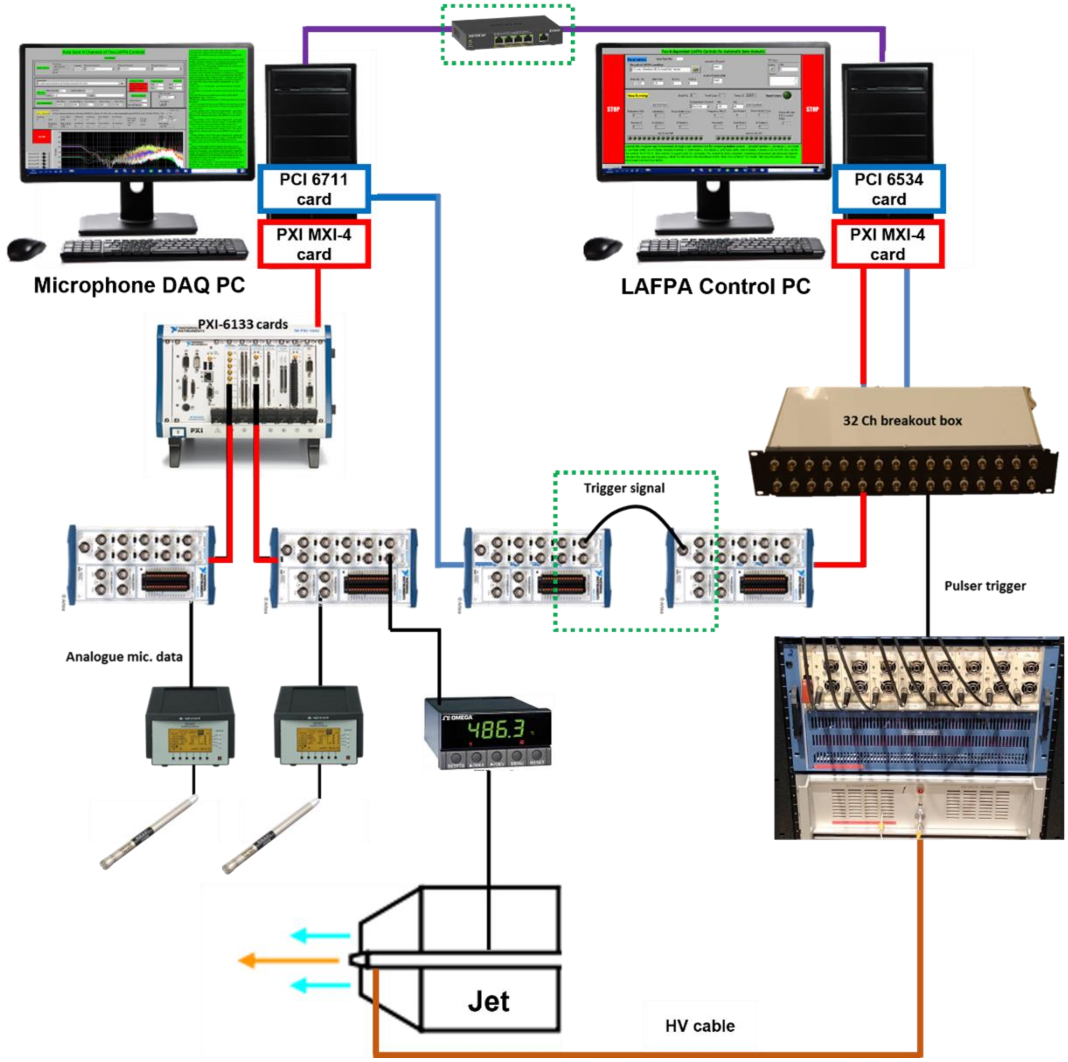

Figure 2.9: Schematic of DAQ for microphones, thermocouple, and LAFPAs

Chapter 3: Empirical Prediction of Shock Locations

3.1 Literature Review

The following method of shock location prediction is an expansion upon the work of Prandtl and his now famous "Prandtl Formula." In 1904, Prandtl developed a formula based on small perturbation theory for the "wavelength" – initial shock cell location – of a nearly ideally expanded axisymmetric supersonic jet (Equation 4) where d_w is the nozzle diameter for a converging nozzle or the throat diameter for a C-D nozzle and $\frac{w_m}{c}$ is the mean flow Mach number with respect to the ambient speed of sound, c.

$$L = 1.306 d_w \sqrt{\left(\frac{w_m}{c}\right)^2 - 1} \tag{4}$$

The coefficient 1.306 comes from the first term of the Bessel series; at the time further terms could not reasonably be computed [24] . Years earlier, Emden developed a similar formula using pressure ratio in place of Mach number (although they were functionally identical) specifically for choked jets [25]. Much of the work in this area noted peculiar regularly spaced discs within the jet which, of course, we know now were shock cells [26].

In 1950, Pack, refined Prandtl's coefficient of 1.306 to 1.22, estimating the first 40 terms of the Bessel series using an early computer. This value applied well to experimental data but seemingly only for the initial shock cell [27]. Sometime later

Harper-Bourne, in a paper investigating the sources of jet noise, found that a value of 1.1 sufficed for the initial coefficient when using a convergent nozzle. It was also noted that the distance between shocks seemed to decrease downstream by about 6% per shock when compared to the initial shock distance [28]. More recently, Mancinelli et al., in an effort to predict screech tones, used the original statement of Prandtl's formula (Equation 4) and a spacing coefficient based on the work of Harper-Bourne to predict shock locations in a convergent nozzle. They introduce a spacing coefficient α and used an average value of 0.06 from Harper-Bourne [29]. Equation 5 shows their equation for the initial shock and Equation 6 describes all subsequent shocks n. These distances are normalized by nozzle diameter.

$$L_1 = 1.306\sqrt{M_j^2 - 1} \tag{5}$$

$$L_n = L_1((1 - \alpha)n + \alpha) \tag{6}$$

Although many of these previous analyses have used convergent nozzles, the derivation of Prandtl's formula does not exclude C-D nozzles – which were used in this work at the GDTL [26]. Hereafter, κ is used to represent the coefficient in the initial shock equation as this value varies with M_j which agrees with trends in literature; most previous studies were performed over Mach number ratios narrow enough that an average value sufficed.

3.2 Methodology

3.2.1 Schlieren Images

Experimental shock locations were determined by analyzing time-averaged schlieren images at each M_j tested. M_j values of 1.30-1.90 were explored in 0.05 increments excluding $M_j = 1.50$ and $M_j = 1.55$ due to their relatively weak shock structure. Shock locations appear on schlieren images (in the configuration used) as sharp transitions from white, signifying less dense air, to black, more dense air. Early shocks are generally very sharp, but shock cells further downstream get muddled due to turbulent mixing (See Figure 3.1). Shock locations measured downstream may, for this reason, be less accurate. Shock cells 1-5 were analyzed; after the 5th shock cell, the jet column is mostly dominated by turbulence. Distances were converted from pixels to inches using the known nozzle height. Hereafter, all shock locations are nondimensionalized by D_e.

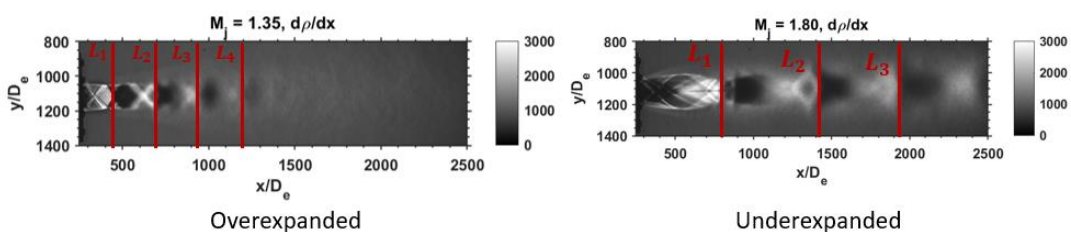

Figure 3.1: Sample schlieren images for overexpanded and underexpanded flow showing shock locations

3.2.2 Analysis of the Results

This method builds on the idea of the two-coefficient fit proposed by Mancinelli. However, instead of attempting to analytically determine physics-based coefficients, an empirical analysis was performed[1]. The method itself is very simple, but many slight variations were explored in order to most efficiently determine the shock locations. A range of both κ and α values were analyzed for each M_j. A range of 0-2 was analyzed for κ with a step size of 0.01. For α, a range of -3 to 3 was used with the same step size. These bounds were chosen based on early results and were reduced from an original range of -10 to 10 with a 0.01 step size in order to reduce computing time. Negative values for κ were not used as a negative initial shock location is nonphysical for the flows explored in this study. For every possible combination of α and κ shock locations were calculated for each M_j using the same equations as Mancinelli but with a variable initial shock coefficient [29].

$$L_1 = \kappa\sqrt{M_j^2 - 1} \tag{7}$$

$$L_n = L_1((1-\alpha)n + \alpha) \tag{8}$$

For each combination, the predicted values were compared to the experimental values using the L2 norm shown in Equation 9 below.

$$\|Error\|_2 = \sqrt{\sum_{n=1}^{m}\left(L_{n,predicted} - L_{n,experimental}\right)^2} \tag{9}$$

The combinations which minimized this value were chosen as the "best" coefficients for each M_j. Predicted shock locations were then calculated using these

---

[1] Because Prandtl originally developed this model using small perturbation theory, which does not apply for cases not very near to the ideally expanded Mach number, the equation is essentially empirical in and of itself. It just so happens that shock locations vary with $\sqrt{M_j - 1}$ and coefficient values around 1.2 coincidentally serve as good estimates in off-design conditions [27].

coefficients for each M_j. The best coefficients were also fit with a linear regression with respect to M_j. Based on initial results, several different methods of coefficient estimation were explored for both underexpanded and overexpanded flow regimes in order to both maximize accuracy and ease of application.

3.2.3 Flow Regime Considerations

This method of shock location estimation was largely developed based on underexpanded flows in which the flow passes through an expansion fan at the nozzle exit before an oblique shock. The first shock cell occurs at this oblique shock. In overexpanded flows, there is no expansion fan at the nozzle exit, just an oblique shock, meaning the initial shock occurs much further upstream. This method is not well-equipped to capture this behavior. The closer initial shock alters the downstream predictions and makes the whole shock train less accurate. As such, an alternate but similar method was explored in the overexpanded regime.

It is proposed that when determining the best coefficients for overexpanded flows, the initial shock (L_1) be used as the origin from which the remainder of the shock cells are measured. Now, what was the second shock (L_2) becomes $L_1{}'$. The best coefficients are calculated using this new coordinate system with L_1 excluded. Then, the predicted value of L_1 is estimated by ${}^{L'_1}/_2$. This, although assuming an equal shock spacing between the first two shocks, improves accuracy in comparison to the original method.

3.3 Results

Initial results showed that coefficients which gave accurate predictions for one flow regime did not necessarily transfer well to the other. Because of this, the flow regimes were analyzed independent of one another. The experimental shock location data was averaged based on schlieren images from two separate dates and is tabulated in Appendix A. Appendix B lists the coefficients used in each prediction iteration at each M_j, R^2 values, and L2 error norms. Appendix B also shows the predicted shock values for every combination of coefficients analyzed in Figure B.1 through Figure B.14.

3.3.1 Underexpanded Regime

In the underexpanded regime, coefficients which minimized error yielded strikingly accurate results. Over all underexpanded Mach numbers analyzed, predictions made using the best coefficients averaged an R^2 value of 0.9994. It was found that κ had a strong linear relationship with M_j ($R^2 = 0.9206$), however, α, did not ($R^2 = 0.2820$). Predictions made using coefficients calculated purely from the linear fits with M_j had an average R^2 value of 0.9993, a negligible difference from the best coefficients. Generally, best κ values varied in magnitude much more than α with ranges of $1.039 - 1.218$ and $-0.0887 \ - \ 0.0028$ respectively.

In subsequent iterations, a value of $\alpha = 0$ was used which had been used for underexpanded flows and yielded accurate predictions in the past [27]. The best values for κ with this set α value were recalculated and refit with M_j. Without the spacing coefficient, the linear relationship between κ and M_j is stronger than the previous fit, with $R^2 = 0.9949$ (See Figure 3.2). Predictions using κ from the linear fit and $\alpha = 0$ were most accurate, although by a statistically insignificant margin (average $R^2 = 0.99946$). Table 1 gives a statistical summary of each iteration showing average R^2 and L2 error norm.

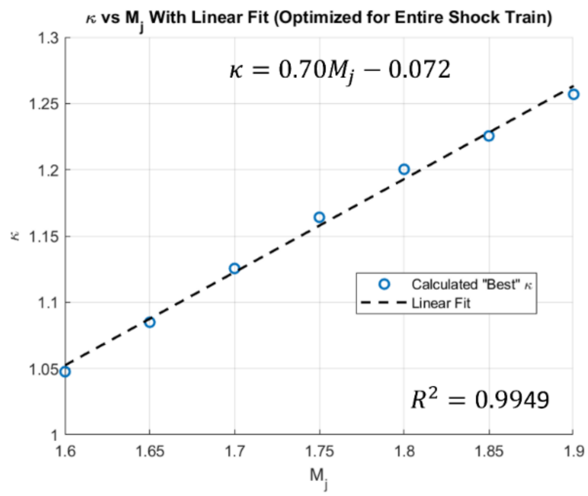

Figure 3.2: Linear fit κ with M_j using $\alpha = 0$ for underexpanded regime

Table 1: Statistical summary of underexpanded flow predictions

Method	**Average R^2**	**Average $\|\|\text{Error}\|\|_2$**
Best Coefficients	0.99938	0.12882
Linear Fit κ & α	0.99926	0.14393
Linear Fit κ, $\alpha = 0$	0.99946	0.12142

3.3.2 Overexpanded Regime

Overexpanded predictions were made through a similar, although more thorough, iterative process using the *same* equations as the underexpanded regime. Again, the best coefficients performed well with an average R^2 of 0.99708 but a slightly higher L2 error norm in comparison to the best coefficients' underexpanded regime predictions. Similar results were achieved using a linear fit for both coefficients although α did not show a strong linear correlation with M_j as shown in Figure 3.3.

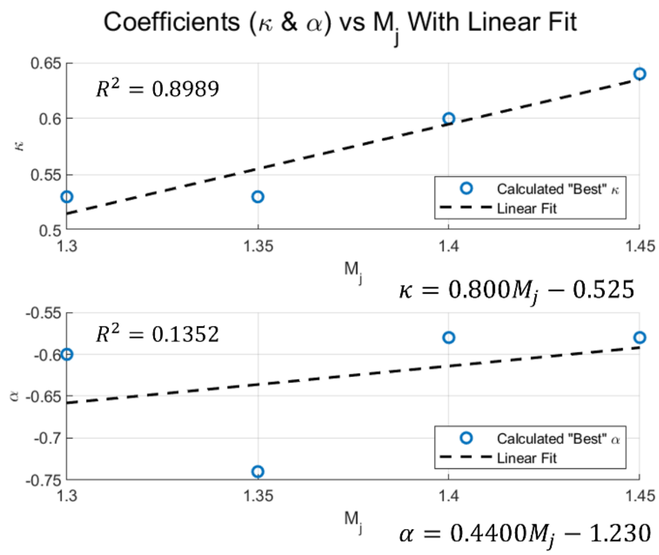

Figure 3.3: Linear fit for best overexpanded coefficients with respect to M_j

Using κ values from the linear fit with an averaged α (because there was no clear trend with M_j) gave similarly accurate results with a slightly higher error norm. Best coefficient values at $M_j = 1.35$ notably depart from the upward trend of other M_j. The linear fit was recalculated excluding the coefficient at $M_j = 1.35$. The linear fit was stronger for both α and κ and the predicted shock values had slightly lower error norms compared to overall linear fit (See Figure 3.4).

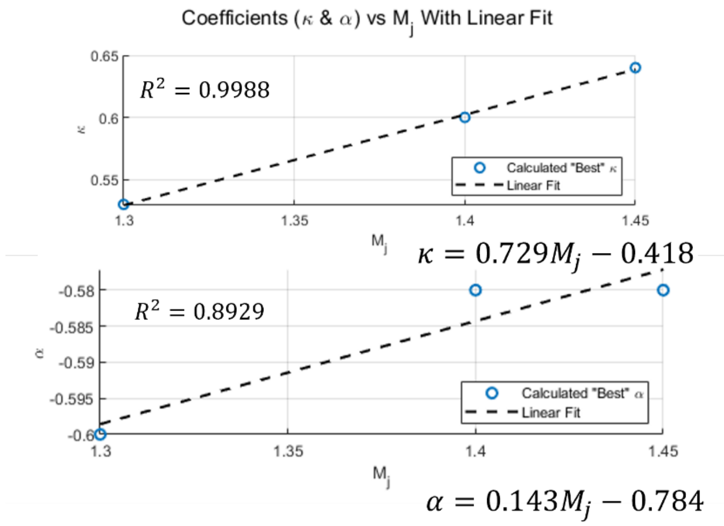

Figure 3.4: Linear fit for best overexpanded coefficients with respect to M_j excluding $M_j = 1.35$

The $\alpha = 0$ case which performed well in the underexpanded regime was underwhelming. Both best κ values and linear fit κ were analyzed, both yielding average error norms over double all other methods explored. Predictions using the alternate method described in 3.2.3 performed well also and yielded the lowest error norms and highest R^2s of any of the approaches.

Table 2: Statistical summary of overexpanded flow predictions

Method	**Average R^2**	**Average $\|\|\text{Error}\|\|_2$**
Best Coefficients	0.99708	0.15033
Linear Fit κ & α	0.99694	0.15363
Linear Fit κ, Average α	0.99619	0.17186
Linear Fit κ & α (No $M_j = 1.35$)	0.99691	0.15497
Best κ, $\alpha = 0$	0.98375	0.35607
Linear Fit κ, $\alpha = 0$	0.98368	0.35691
Alternate Method – Best Coefficients	0.99749	0.13838
Alternate Method – Linear Fit κ, Average α	0.99749	0.13913
Alternate Method – Best κ, $\alpha = 0$	0.99501	0.19598

3.4 Discussion

Initially, coefficient values reported from literature were used as a first-order estimate which predicted shock location very poorly likely due to the nozzle geometry, as they were developed for circular jets. Previous work has almost exclusively focused on underexpanded circular jets. It is notable that the κ values in the underexpanded regime are similar to those used by Prandtl and Pack, 1.306 and 1.22 respectively [24], [27]. Best κ values ranged from approximately 1.0 - 1.2. Nearly all best α values were negative but on the order of magnitude of the 0.06 found by Harper-Bourne [28]. The negative value indicates that the distance between subsequent shocks was increasing which was the case for moderately underexpanded Mach numbers ($1.50 < M_j < 1.70$) although only slightly. The relatively small values of best α compared to κ and the nearly constant distance between shocks in this regime reduced reliance on α. As reported, the most accurate predictions came from predictions made with κ given by the linear fit and $\alpha = 0$. Substituting the linear fit into the original shock location formula yields the following equation – a highly accurate empirical prediction of underexpanded shock locations for the nozzle geometry used.

$$L_n = n\left(0.70M_j - 0.072\right)\sqrt{M_j^2 - 1} \tag{10}$$

This same equation does not apply to the overexpanded regime. In fact, it performs quiet poorly. Overall, the overexpanded predictions were slightly less accurate and had slightly higher error norms. That said, predictions still performed very well. Using the non-altered method, κ values were much lower compared to those in the underexpanded regime, ranging from approximately 0.5 - 0.6. These lower κ values are compensated for by much larger α values for the best coefficients. α values for non-altered cases were an order of magnitude larger for the overexpanded regime. This is due to the different flow physics between the two regimes. The κ values being roughly half of those in the underexpanded regime is a direct consequence of the closer first shock to the nozzle exit. The larger α values compensate for the much reduced initial shock location. However, using the altered method, κ values range from roughly 0.9-1.2, very similar to the underexpanded regime. Spacing coefficients found with this method are much reduced but stay fairly constant around 0.18. The altered method is slightly more accurate than the traditional technique, specifically when using κ from the linear fit and an average α of 0.178. Substituting these values into the original shock equations gives the following slightly more cumbersome equations. These empirical equations capture a phenomenon which the original set do not however.

$$L_1 = (0.63M_j - 0.3225)\sqrt{M_j^2 - 1} \tag{11}$$

$$L_n = L_1(1.644n - 0.288) \text{ for } n > 1 \tag{12}$$

Because all results were normalized by equivalent nozzle diameter, it is expected that these estimate would perform well for any supersonic jet. Also, it should be noted that, experimental shock locations vary by up to 5% between data sets. All methods analyzed were comfortably within that margin of error. Those presented in this final subsection balanced both accuracy and ease of implementation for the purposes of implementation in the earlier discussed screech closure model.

Chapter 4: Prediction of Convective Velocity Using Empirical Mode Decomposition

4.1 Literature Review

4.1.1 Near Field Pressure Decomposition

Work by Arndt et al. and Coiffet et al. has shown that the irrotational near field pressure carries information on turbulent structures within a jet [30], [31]. This convecting turbulence makes up the hydrodynamic component of the pressure. Superimposed over the hydrodynamic pressure fluctuations are acoustic pressure fluctuations which propagate spherically outward at sonic speed [32]. These pressure components can be decomposed to isolate the hydrodynamic fluctuations which reveals information about the turbulent structures convecting downstream [33]. Figure 4.1 shows a spectrum of sample near field pressure data and highlights the difference in waveform shape for acoustic and hydrodynamic components. Work by Crawley et al. [34] at the GDTL has focused extensively on the decomposition of the irrotational near field pressure components using three different methods to varying degrees of success: multidimensional Fourier transform, continuous wavelet transform, and Empirical Mode Decomposition (EMD). EMD is the method explored in this work and it was found to have performed well if the two pressure components were distinct, which is admissible for the purposes of estimating convective velocity. Using EMD to decompose near field pressure components was first proposed by Kuo et al. [35].

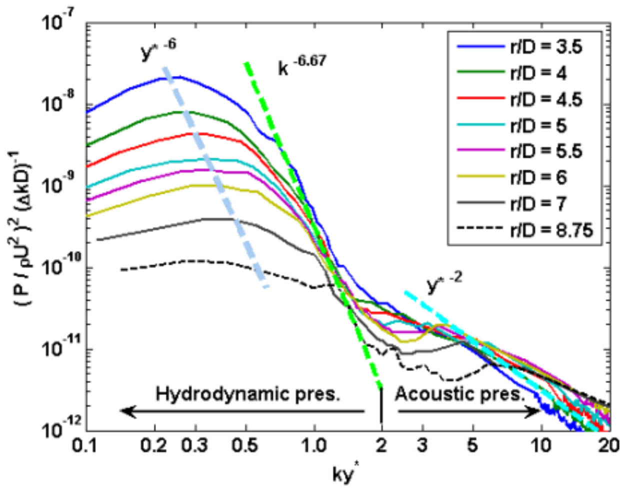

Figure 4.1: Normalized near field pressure plotted against wavenumber (frequency analog) at different radial microphone positions) [35]

4.1.2 Convective Velocity Estimation

Relatively little research has been conducted on the estimation of the convection speed of LSS in supersonic jets. Much of what has been done has been exploratory and focused mostly on validating new methods. There is, at this time, no tried and true method to estimate convective velocity in a supersonic flow. Much previous work involves detailed analysis of high-speed schlieren images or the measurement of phase shift between two sensors at various axial distances [36]. Typical values for U_c/U_j range from 0.4-0.85 for an unheated supersonic jet [37].

4.1.3 Empirical Mode Decomposition

EMD is a time-frequency data analysis method that was specifically developed to analyze nonlinear and non-stationary data. It was introduced as an alternative to Fourier spectral analysis which is limited to both linear and stationary signals [38]. However, whereas Fourier transforms can only output sine or cosine waves, EMD analysis allows a physically-meaningful output which can vary in both instantaneous frequency and amplitude over the full frequency range of a signal. This algorithm outputs several distinct Intrinsic Mode Functions (IMFs). IMFs must satisfy two mathematical criteria as proposed by Huang et al.: “(1) in the whole data set, the number of extrema and the number of zero crossings must either equal or differ at most by one; and (2) at any point, the mean value of the envelope defined by the local maxima and the envelope defined by the local minima is zero” [38].

A simplified form of the EMD algorithm is as follows: find the local minima and maxima of an input signal $x(t)$, use those local minima and maxima to create envelopes of $x(t)$ and also to create a mean envelope. The output function is the residual $Y(t) = x(t) - m(t)$. This process is known as *sifting*. This is repeated several times using the residual signal $Y(t)$ as the new input signal $x(t)$ until one of several criteria are met. Each repetition of the process creates a new “mode.” Each of these constructed modes is an IMF [39]. The exit criteria used in this work was the maximum allowed number of IMFs. A maximum of 7 IMFs was used based on similar work by Crawley et al. [40].

4.2 Post-Processing

4.2.1 Separating Hydrodynamic & Acoustic Pressure Components

Pressure data for each microphone was decomposed separately. A scaling factor of 1000 was applied and then MATLAB’s “emd” function was used to decompose the raw signal of each microphone into 7 IMFs. The power spectral density (PSD) was calculated for each IMF. IMF’s whose spectral maximum, disregarding the screech tone and its harmonics, occurred at a frequency greater than some critical frequency were designated acoustic. A moving median filter was used to smooth screech tones from the spectrum so that IMFs could accurately be categorized. The feasibility of this sorting method was confirmed via manual checks for several microphones at each M_j analyzed. Figure 4.2 below shows both the raw and smoothed IMFs along with their categorization. The raw – unsmoothed – hydrodynamic IMFs were summed and used for cross-correlation later on.

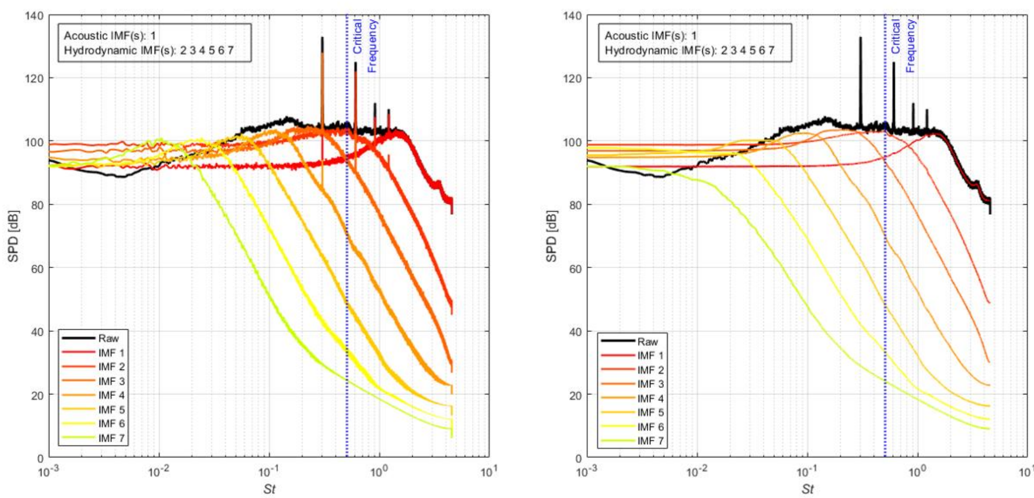

(a) (b)

Figure 4.2: Decomposed near field pressure data from mic. 7 at $M_j = 1.50$: a) Raw IMFs; b) IMFs smoothed using moving median filter for decomposition

The criteria used for critical frequency is defined by Sinha et al. as $f_{crit} = U_c/y$ where y is the y-location of the microphone analyzed with respect to the centerline of the jet [41]. Previous work has used a critical wavenumber ky^* as proposed by Kuo et al. where $k = 2\pi f_{crit}/a_0$ [35]. However, it's been found that the former definition performs well over a range of Mach numbers and produces comparable results. Estimates of U_c

based on concurrent work in the GDTL were used as a first-order estimate of critical frequency.

4.2.2 Filtering & Cross Correlation

The decomposed pressure data was filtered to remove the screech tone using a bandstop filter at ± 400 Hz around the screech tone along with a lowpass filter which filtered data just prior to and beyond the first harmonic. While this did remove the screech tone, it also nearly flattened the spectral waveform at frequencies above the fundamental tone, removing the $k^{-6.67}$ decay shown in Figure 4.2. Figure 4.3a shows a sample filtered waveform in comparison to the unfiltered hydrodynamic pressure. Various other methods of filtering were explored including a wavelet synchrosqueezed transform (WSST). WSST is similar in function to EMD and can be used to remove specified modes within a defined frequency range of a signal [42]. While this method was partially successful it could not completely remove the screech tone. A frequency range on the order of 1000 Hz was necessary in order to effectively remove the tone. At this range, the shape of the spectrum surrounding the screech tone was drastically altered. Figure 4.3b shows a hydrodynamic signal filtered with WSST with a frequency range of 600 Hz where the screech tone is still largely present although slightly diminished.

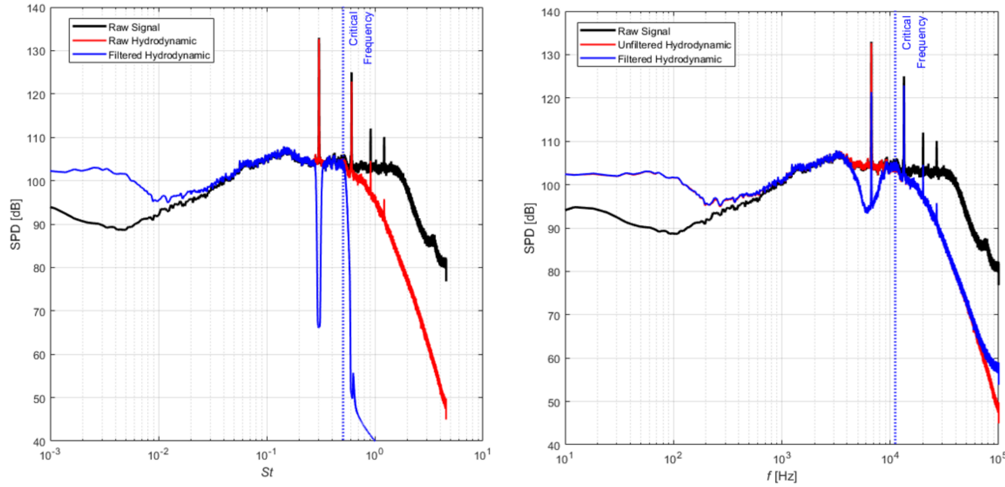

(a) (b)

Figure 4.3: a) Hydrodynamic pressure component with bandstop filter applied at screech frequency and lowpass filter slightly before the first harmonic; b) hydrodynamic signal filtered using WSST at 600 Hz range around screech tone

At each M_j, cross correlations were calculated between all microphones in the array downstream of a specified reference microphone using MATLAB's "xcorr" function. Microphone 4 was used as the reference microphone for all estimations. At microphones further upstream, the turbulent structures are not sufficiently developed (See Figure 4.4). Cross correlations between each possible combination of microphones in the linear array downstream of the reference microphone were calculated. The lags between structures which showed high correlations were then used to calculate U_c based on the known microphone spacing. All U_c results were normalized with U_j based on the jet total temperature and Mach number.

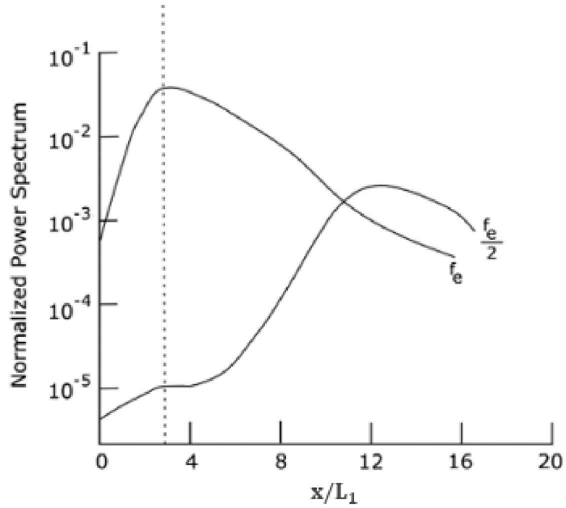

Figure 4.4: Streamwise normalized power spectrum showing vortex roll up after roughly 3 shocks, adapted from Samimy et al. [43]

Possible variation of U_c due to the finite microphone diameter (6.35 mm) determined error bars for each estimated U_c. If the difference in estimated minimum and maximum U_c exceeded $0.1U_j$ a data point was considered inadmissible. Additionally, nonphysical values were not considered ($U_c < 0$). If the maximum correlation between two microphones occurred before 0.1 ms data point was not considered. This usually occurred between a pair of adjacent microphones due to their proximity. Estimations which met all other conditions but did not fall into the range $0.4 \leq {U_c}/{U_j} \leq 0.8$ were not dismissed but may be inaccurate.

4.3 Results

Figure 4.5 shows a sample of correlation data for $M_j = 1.50$ between each possible microphone pair using microphone 4 as the reference. Many of the estimated U_c values did not meet the set admissibility criteria. In adjacent pairs, the delay was almost always shorter than the set value of 0.1 ms. Figure 4.6 shows the axial convective velocity estimation at the same Mach number. Generally, microphones further away from one have smaller error bars than pairs near one another.

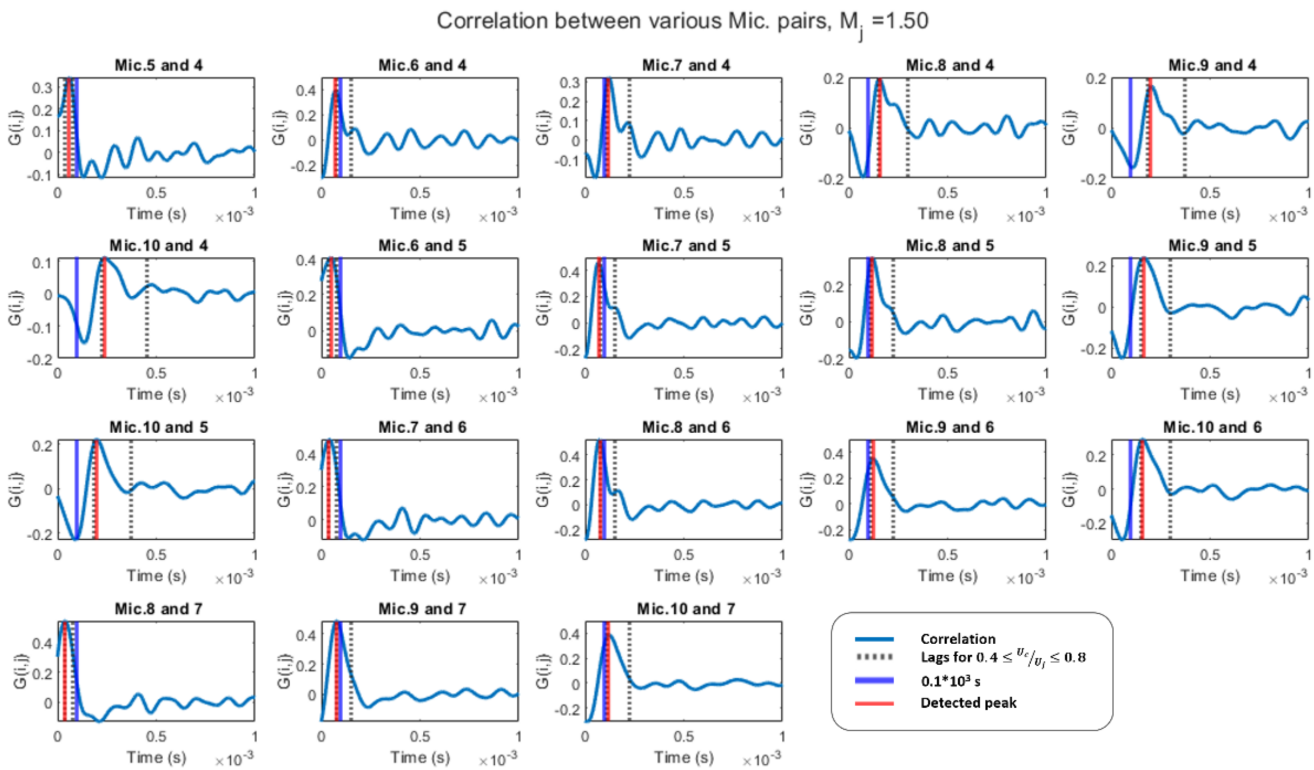

Figure 4.5: Correlations between microphone pairs at $M_j = 1.50$ showing admissibility criteria

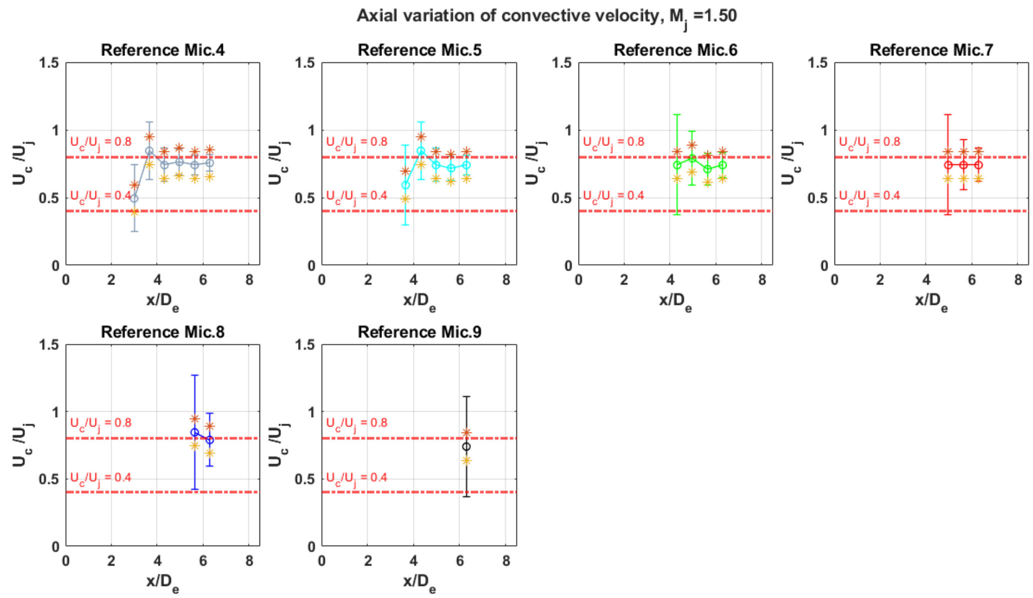

Figure 4.6: Axial convective velocity estimations for $M_j = 1.50$

Figure 4.7 shows the admissible U_c estimations for all Mach numbers analyzed. Values estimated using both decomposed and nondecomposed pressure components are shown along with the U_c estimations used to calculate critical frequency. For a set M_j, convective velocity estimations showed large variations with streamwise distance. At strongly underexpanded Mach numbers the amount of admissible data points reduced significantly. The U_c/U_j estimates made using decomposed pressure data are consistently less than the U_c estimate values. However, both consistently decrease with rising Mach number.

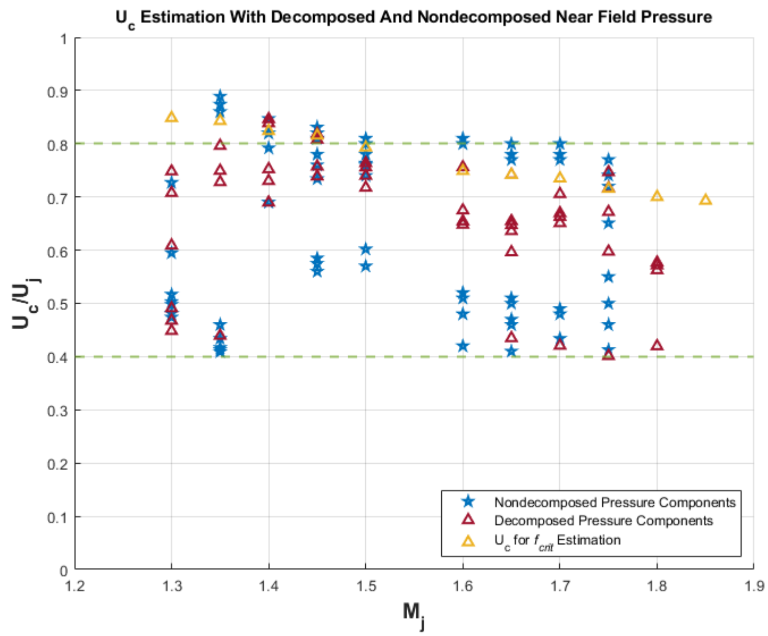

Figure 4.7: Admissible U_c estimations calculated using separated and unseparated pressure components compared to expected results

4.4 Discussion

The variation in results and amount of inadmissible data points has several likely causes. Some of the issues presumably stem from the method used to remove the screech tone and its harmonics from the hydrodynamic signal. As noted before, the filtering process used drastically alters the shape of the waveform. This phenomenon becomes worse at strongly underexpanded Mach numbers. Figure 4.8 shows the filtered hydrodynamic signal at $M_j = 1.85$. Note, the bandstop filter designed to remove the screech tone has affected the entire range of Strouhal numbers from 0.01 to the screech tone at approximately 0.2. Then, the low pass filter drastically reduces SPD at frequencies greater than the first harmonic, removing the expected decay (See Figure 4.1).

Generally, the estimations do follow the expected trends from literature. U_c/U_j decreases for higher M_j. For most Mach numbers analyzed, with the exception of $M_j = 1.75$, values cluster with a few outliers. The screech closure model requires a single averaged value. Based on the current results, an average may not give the best results due to the number of unacceptable data points and the microphone array does not have the spatial resolution required to give accurate estimations further upstream due to the earlier-described effect between adjacent pairs.

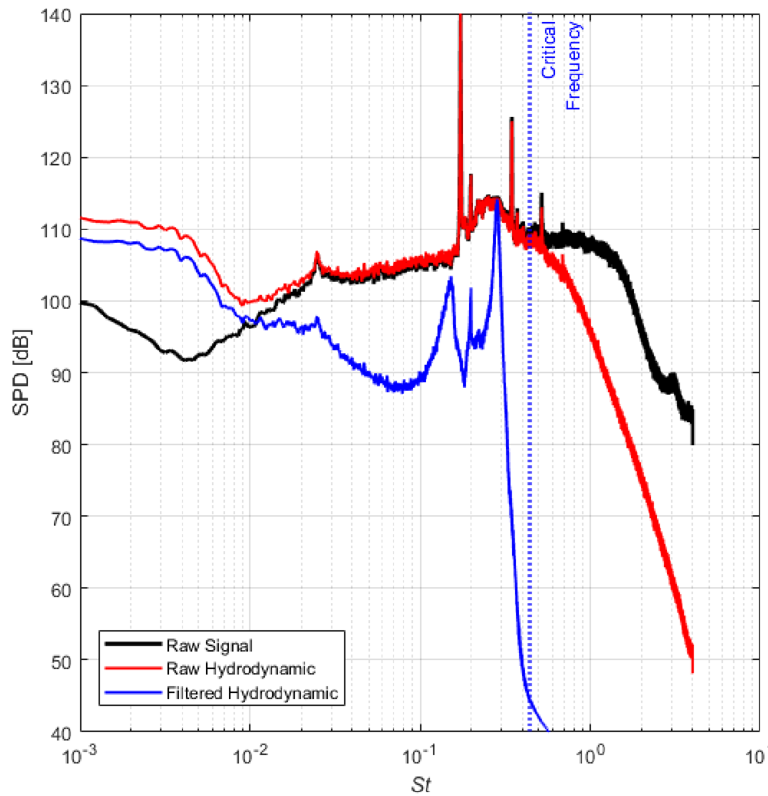

Figure 4.8: Filtered hydrodynamic pressure component SPD versus Strouhal number at $M_j = 1.85$

Chapter 5: Conclusions

5.1 Summary

Two parameters were estimated to aid the development of a physics-based screech closure model for a supersonic rectangular twin jet configuration. Locations of shocks within the jet flow were predicted via an empirical method established by Prandtl and built upon by researchers over the course of the 20th century. Additionally, the velocity at which large-scale turbulent structures in the jet mixing layer convect downstream was estimated using decomposed near field hydrodynamic pressure data from a linear microphone array.

Normalized shock location predictions solely as a function of M_j proved highly accurate compared to experimental data from time-averaged schlieren images for the entire range of Mach numbers analyzed. In order to improve predictions, the underexpanded and overexpanded regimes were analyzed separately. In the underexpanded regime, results were similar to those obtained by previous researchers working with axisymmetric converging jets. In the overexpanded regime, a slightly altered method was explored after less accurate initial results. The altered method – which accounts for the different flow physics between the two regimes – performed well and at the same order of accuracy as the underexpanded regime. Results in both regimes showed less variation from the averaged experimental data than the data sets did from one another. The final shock location equations presented have been optimized for the specific jet configuration analyzed but a similar analysis could be performed for other nozzle geometries.

Convective velocity estimations used two different configurations of streamwise linear microphone arrays to capture near field pressure data in the overexpanded and underexpanded regimes. Pressure data was decomposed into hydrodynamic and acoustic components using EMD which previous research has proven reasonably effective. Pressure data from each microphone was split into 7 IMFs which were designated hydrodynamic if their smoothed peak occurred at a frequency less than some critical frequency. This critical frequency was based on microphone position and approximate values of U_c. Convective velocity was calculated using the time difference between microphone cross correlations for the summed hydrodynamic components. Estimated U_c values followed expected trends for the most part but at higher underexpanded Mach numbers erroneous data points began to dominate. Both components of this work meaningfully contribute to the development of a screech closure model for the rectangular twin jet configuration.

5.2 Future Work

5.2.1 Shock Location Prediction

The empirical method of shock location prediction examined was highly accurate. Future iterations should focus on practical implementation and determine what level of accuracy is truly necessary – especially for the purposes of developing a screech and coupling model. Instead of a shock equation for each flow regime, perhaps one could develop a single equation which predicts shock locations at a lower accuracy for the entire range of Mach numbers explored.

5.2.2 Convective Velocity Estimation

Although decomposition of irrotational pressure components has been proven successful in the past, its validity should be confirmed for this specific application. Additionally, future work should determine a more precise and less destructive method of removing the screech tone and its harmonics from the decomposed hydrodynamic pressure data. The current method fundamentally alters the waveform shape which could result in inaccurate convective velocity estimations. This issue seems to be exacerbated at strongly underexpanded Mach numbers. Additionally, the pressure components were decomposed using a critical frequency estimate based on a first guess of U_c. Future work should iteratively determine f_{crit} until some convergence criterion is reached.

References

[1] B. S. Henderson and D. L. Huff, "A history of jet noise research at the National Aeronautics and Space Administration," *The Journal of the Acoustical Society of America*, vol. 150, no. 2, pp. 1346–1369, Aug. 2021, doi: 10.1121/10.0005891.

[2] M. Kandula and B. Vu, "On the Scaling Laws for Jet Noise in Subsonic and Supersonic Flow," presented at the 9th AIAA/CEAS Aeroacoustics Conference and Exhibit, Hilton Head, South Carolina, May 2003. doi: 10.2514/6.2003-3288.

[3] D. L. Huff, "Noise Reduction Technologies for Turbofan Engines," E-15787, Sep. 2007. Accessed: Mar. 30, 2022. [Online]. Available: https://ntrs.nasa.gov/citations/20080001448

[4] B. Ferguson, *Chevrons on Boeing 777*. [Photo]. Available: https://www.nasa.gov/images/content/505606main_qtd2_sunrise_3024x2016.jpg

[5] A. Esfahani, N. J. Webb, and M. Samimy, "Coupling Modes in Supersonic Twin Rectangular Jets," presented at the AIAA SciTech 2021 Forum, Virtual, Jan. 2021. doi: 10.2514/6.2021-1292.

[6] J. D. Anderson, *Modern compressible flow: with historical perspective*, 3rd ed. Boston: McGraw-Hill, 2003.

[7] T. Landis, *J58 Turbojet in Full Afterburner*. 1997. [Photo]. Available: https://images.nasa.gov/details-EC97-44007-01

[8] C. duP. Donaldson and R. S. Snedeker, “A study of free jet impingement. Part 1. Mean properties of free and impinging jets,” *J. Fluid Mech.*, vol. 45, no. 02, p. 281, Jan. 1971, doi: 10.1017/S0022112071000053.

[9] C. K. W. Tam, “Supersonic Jet Noise,” *Annu. Rev. Fluid Mech.*, vol. 27, no. 1, pp. 17–43, Jan. 1995, doi: 10.1146/annurev.fl.27.010195.000313.

[10] A. Powell, “On the Noise Emanating from a Two-Dimensional Jet Above the Critical Pressure,” *Aeronautical Quarterly*, vol. 4, no. 2, pp. 103–122, Aug. 1953, doi: 10.1017/S0001925900000822.

[11] J. Seiner, “Advances in high speed jet aeroacoustics,” in *9th Aeroacoustics Conference*, American Institute of Aeronautics and Astronautics, 1984. doi: 10.2514/6.1984-2275.

[12] C. S. Kim, S. T. Grady, J. E. Hart, F. Laden, T. VoPham, D. D. Nguyen, J. E. Manson, P. James, J. P. Forman, K. M. Rexrode, *et al.*, “Long-term aircraft noise exposure and risk of hypertension in the Nurses’ Health Studies,” *Environ Res*, vol. 207, p. 112195, May 2022, doi: 10.1016/j.envres.2021.112195.

[13] K. Dimakopoulou, K. Koutentakis, I. Papageorgiou, M.-I. Kasdagli, A. S. Haralabidis, P. Sourtzi, E. Samoli, D. Houthuijs, W. Swart, A. L. Hansell, and K. Katsouyanni, “Is aircraft noise exposure associated with cardiovascular disease and

hypertension? Results from a cohort study in Athens, Greece," *Occup Environ Med*, vol. 74, no. 11, pp. 830–837, Nov. 2017, doi: 10.1136/oemed-2016-104180.

[14] N. C. Schaal, R. A. Salaam, M. E. Stevens, and A. H. Stubner, "Living at Work: 24-hour Noise Exposure Aboard US Navy Aircraft Carriers," *Annals of Work Exposures and Health*, vol. 63, no. 3, pp. 316–327, Mar. 2019, doi: 10.1093/annweh/wxz005.

[15] J. S. Mixson and L. A. Roussos, "Acoustic fatigue: Overview of activities at NASA Langley," NASA-TM-89143, Apr. 1987. Accessed: Mar. 30, 2022. [Online]. Available: https://ntrs.nasa.gov/citations/19870015532

[16] G. Raman, "Supersonic Jet Screech: Half-Century from Powell to the Present," *Journal of Sound Vibration*, vol. 225, pp. 543–571, Aug. 1999, doi: 10.1006/jsvi.1999.2181.

[17] R. Shenk, *F-22 Raptor*. 2008. [Photo]. Available: https://www.flickr.com/photos/rcsj/2504022678/

[18] C. Wiegand, "F-35 Air Vehicle Technology Overview," in *2018 Aviation Technology, Integration, and Operations Conference*, American Institute of Aeronautics and Astronautics, 2018. doi: 10.2514/6.2018-3368.

[19] A. G. Esfahani, N. J. Webb, and M. Samimy, "Control of Coupling in Twin Rectangular Supersonic Jets," in *AIAA AVIATION 2021 FORUM*, American Institute of Aeronautics and Astronautics. doi: 10.2514/6.2021-2122.

[20] D. Edgington-Mitchell, V. Jaunet, P. Jordan, A. Towne, J. Soria, and D. Honnery, "Upstream-travelling acoustic jet modes as a closure mechanism for screech," *Journal of Fluid Mechanics*, vol. 855, Nov. 2018, doi: 10.1017/jfm.2018.642.

[21] A. Powell, "The Noise of Choked Jets," *The Journal of the Acoustical Society of America*, vol. 25, no. 3, pp. 385–389, May 1953, doi: 10.1121/1.1907052.

[22] C. B. Hahn, "Design and Validation of the New Jet Facility and Anechoic Chamber," The Ohio State University, 2011. Accessed: Apr. 02, 2022. [Online]. Available: https://etd.ohiolink.edu/apexprod/rws_olink/r/1501/10?clear=10&p10_accession_num=osu1311877224

[23] C. B. Hahn, M. Kearney-Fischer, and M. Samimy, "On factors influencing arc filament plasma actuator performance in control of high speed jets | SpringerLink," *Experiments in Fluids*, vol. 51, no. 6, pp. 1591–1603, 2011, doi: 10.1007/s00348-011-1172-5.

[24] L. Prandtl, "Über die stationären Wellen in einem Gasstrahl (Stationary waves in a gaseous jet)," *Phys. Z*, vol. 5, pp. 599–601, 1904.

[25] R. Emden, "Über die Ausstromungserscheinungen permanenter Gase," *Physik*, vol. 69, pp. 426–453, 1899.

[26] A. Powell, "On Prandtl's Formulas for Supersonic Jet Cell Length," *International Journal of Aeroacoustics*, vol. 9, no. 1–2, pp. 207–236, Jan. 2010, doi: 10.1260/1475-472X.9.1-2.207.

[27] D. C. Pack, “A note on Prandtl’s formula for the wave-length of a supersonic gas jet,” *The Quarterly Journal of Mechanics and Applied Mathematics*, vol. 3, no. 2, pp. 173–181, Jan. 1950, doi: 10.1093/qjmam/3.2.173.

[28] M. Harper-Bourne, “The noise from shock waves in supersonic jets-Noise Mechanism-,” *AGARD CP-131*, 1974, Accessed: Apr. 01, 2022. [Online]. Available: https://ci.nii.ac.jp/naid/10021111327/

[29] M. Mancinelli, V. Jaunet, P. Jordan, and A. Towne, “Screech-tone prediction using upstream-travelling jet modes,” *Exp Fluids*, vol. 60, no. 1, p. 22, Jan. 2019, doi: 10.1007/s00348-018-2673-2.

[30] R. E. A. Arndt, D. F. Long, and M. N. Glauser, “The proper orthogonal decomposition of pressure fluctuations surrounding a turbulent jet,” *Journal of Fluid Mechanics*, vol. 340, pp. 1–33, Jun. 1997, doi: 10.1017/S0022112097005089.

[31] F. Coiffet, P. Jordan, J. Delville, Y. Gervais, and F. Ricaud, “Coherent Structures in Subsonic Jets: A Quasi-Irrotational Source Mechanism?,” *International Journal of Aeroacoustics*, vol. 5, no. 1, pp. 67–89, Jan. 2006, doi: 10.1260/147547206775220407.

[32] A. Guitton, P. Jordan, E. Laurendeau, and J. Delville, “Velocity dependence of the near pressure field of subsonic jets: understanding the associated source mechanisms.,” in *13th AIAA/CEAS Aeroacoustics Conference (28th AIAA Aeroacoustics Conference)*, American Institute of Aeronautics and Astronautics, 2007. doi: 10.2514/6.2007-3661.

[33] C. E. Tinney and P. Jordan, “The near pressure field of co-axial subsonic jets,” *Journal of Fluid Mechanics*, vol. 611, pp. 175–204, Sep. 2008, doi: 10.1017/S0022112008001833.

[34] M. Crawley and M. Samimy, “Decomposition of the Near-Field Pressure in an Excited Subsonic Jet,” in *20th AIAA/CEAS Aeroacoustics Conference*, American Institute of Aeronautics and Astronautics. doi: 10.2514/6.2014-2342.

[35] C.-W. Kuo, Q. Buisson, D. K. McLaughlin, and P. J. Morris, “Experimental Investigation of Near-Field Pressure Fluctuations Generated by Supersonic Jets,” in *19th AIAA/CEAS Aeroacoustics Conference*, American Institute of Aeronautics and Astronautics, 2013. doi: 10.2514/6.2013-2033.

[36] T. Castelain, R. Gojon, B. Mercier, and C. Bogey, “Estimation of convection speed in underexpanded jets from schlieren pictures,” in *22nd AIAA/CEAS Aeroacoustics Conference*, American Institute of Aeronautics and Astronautics, 2016. doi: 10.2514/6.2016-2984.

[37] E. Murakami and D. Papamoschou, “Eddy Convection in Coaxial Supersonic Jets,” *AIAA Journal*, May 2012, doi: 10.2514/2.1034.

[38] N. E. Huang, Z. Shen, S. R. Long, M. C. Wu, H. H. Shih, Q. Zheng, N.-C. Yen, C. C. Tung, and H. H. Liu, “The empirical mode decomposition and the Hilbert spectrum for nonlinear and non-stationary time series analysis,” *Proceedings of the Royal Society of London. Series A: Mathematical, Physical and Engineering Sciences*, vol. 454, no. 1971, pp. 903–995, Mar. 1998, doi: 10.1098/rspa.1998.0193.

[39] “Empirical mode decomposition - MATLAB emd.” https://www.mathworks.com/help/signal/ref/emd.html (accessed Apr. 06, 2022).

[40] M. Crawley, C.-W. Kuo, and M. Samimy, “Identification of the acoustic response in the irrotational near-field of an excited subsonic jet,” *International Journal of Aeroacoustics*, vol. 15, no. 4–5, pp. 496–514, Jul. 2016, doi: 10.1177/1475472X16642137.

[41] A. Sinha, H. Alkandry, M. Kearney-Fischer, M. Samimy, and T. Colonius, “The impulse response of a high-speed jet forced with localized arc filament plasma actuators,” *Physics of Fluids*, vol. 24, no. 12, p. 125104, Dec. 2012, doi: 10.1063/1.4772191.

[42] I. Daubechies, J. Lu, and H.-T. Wu, “Synchrosqueezed wavelet transforms: An empirical mode decomposition-like tool,” *Applied and Computational Harmonic Analysis*, vol. 30, no. 2, pp. 243–261, Mar. 2011, doi: 10.1016/j.acha.2010.08.002.

[43] M. Samimy, N. Webb, and M. Crawley, “Excitation of Free Shear-Layer Instabilities for High-Speed Flow Control,” *AIAA Journal*, vol. 56, no. 5, pp. 1770–1791, 2018, doi: 10.2514/1.J056610.

Appendix A: Experimental Shock Locations

Table A.1: Experimental shock locations from August 20th, 2021

M_j		1.20	1.25	1.30	1.35	1.40	1.45	1.65	1.70	1.75	1.80	1.85	1.90
Shock Tip distance from nozzle [in]	1	0.1504	0.2167	0.2983	0.3340	0.3952	0.4589	1.0428	1.1780	1.2162	1.2774	1.3972	1.4967
	2	0.5813	0.7343	0.9179	1.0377	1.1856	1.3335	2.1621	2.3585	2.5624	2.7766	2.9474	3.1234
	3	1.0275	1.2340	1.4814	1.7032	1.9684	2.2386	3.2967	3.6027	3.8500	4.1534	4.4058	4.6302
	4	1.4100	1.7108	1.9811	2.3049	2.6313	2.9525	4.3906	4.7399	5.1249	5.4920	5.8184	6.2161
	5	1.7950	2.1162	2.4120	2.8123	3.1667	3.6052	5.3620	5.9535	6.4430	6.9300	7.3227	7.7842

Table A.2: Experimental shock locations from October 21st, 2021

M_j		1.20	1.25	1.30	1.35	1.40	1.45	1.65	1.70	1.75	1.80	1.85	1.90
Shock Tip distance from nozzle [in]	1	0.1522	0.1991	0.2810	0.3044	0.3513	0.4333	1.0656	1.1710	1.2178	1.2763	1.4052	1.4871
	2	0.5386	0.6674	0.8548	1.0187	1.1710	1.3349	2.1780	2.3419	2.5527	2.7986	2.9977	3.1850
	3	0.9368	1.1827	1.4403	1.6511	1.8735	2.1077	3.2436	3.5129	3.7939	4.0984	4.3560	4.6019
	4	1.2646	1.6393	1.9321	2.2717	2.5995	3.0211	4.3208	4.6487	5.0234	5.3864	5.7260	6.1241
	5	1.7096	2.0375	2.4239	2.8923	3.2084	3.6885	5.3279	5.7143	6.1944	6.6276	7.0492	7.5410

Table A.3: Averaged experimental shock locations

M_j		1.20	1.25	1.30	1.35	1.40	1.45	1.65	1.70	1.75	1.80	1.85	1.90
Shock Tip distance from nozzle [in]	1	0.1513	0.2079	0.2897	0.3192	0.3732	0.4461	1.0542	1.1745	1.2170	1.2769	1.4012	1.4919
	2	0.5600	0.7009	0.8863	1.0282	1.1783	1.3342	2.1701	2.3502	2.5576	2.7876	2.9725	3.1542
	3	0.9821	1.2084	1.4608	1.6771	1.9209	2.1732	3.2701	3.5578	3.8220	4.1259	4.3809	4.6160
	4	1.3373	1.6751	1.9566	2.2883	2.6154	2.9868	4.3557	4.6943	5.0741	5.4392	5.7722	6.1701
	5	1.7523	2.0769	2.4179	2.8523	3.1876	3.6469	5.3449	5.8339	6.3187	6.7788	7.1859	7.6626

Appendix B: Various Shock Location Prediction Results

Table B.1: Summary of underexpanded shock location prediction results

Method	M_j	1.60	1.65	1.70	1.75	1.80	1.85	1.90
Best Coefficients	R^2	0.99959	0.99935	0.99983	0.99964	0.99878	0.99908	0.99939
	$\|\|\text{Error}\|\|_2$	0.08372	0.11430	0.06430	0.10022	0.19912	0.18226	0.15779
	κ	1.039	1.060	1.127	1.118	1.126	1.188	1.218
	α	-0.0106	-0.0312	0.0028	-0.0553	-0.0887	-0.0415	-0.0418
Linear Fit κ & α	R^2	0.99946	0.99939	0.99956	0.99950	0.99888	0.99895	0.99909
	$\|\|\text{Error}\|\|_2$	0.09642	0.11121	0.10263	0.11903	0.19048	0.19470	0.19301
	κ	1.040	1.069	1.097	1.125	1.154	1.182	1.210
	α	-0.0160	-0.0233	-0.0307	-0.0380	-0.0454	-0.0527	-0.0601
Linear Fit κ, $\alpha = 0$	R^2	0.99948	0.99946	0.99978	0.99961	0.99905	0.99937	0.99947
	$\|\|\text{Error}\|\|_2$	0.09434	0.10486	0.07171	0.10543	0.17561	0.14999	0.14800
	κ	1.052	1.088	1.123	1.158	1.193	1.228	1.263
	α	0	0	0	0	0	0	0

Table B.2: Summary of overexpanded shock location prediction results

Method	$\boldsymbol{M_j}$	**1.30**	**1.35**	**1.40**	**1.45**
Best Coefficients	R^2	0.99687	0.99807	0.99612	0.99723
	$\lVert\mathrm{Error}\rVert_2$	0.12448	0.11598	0.18389	0.17697
	κ	0.530	0.530	0.600	0.640
	α	-0.600	-0.740	-0.580	-0.580
Linear Fit κ & α	R^2	0.99678	0.99788	0.99589	0.99723
	$\lVert\mathrm{Error}\rVert_2$	0.12631	0.12161	0.18941	0.17720
	κ	0.515	0.555	0.595	0.635
	α	-0.658	-0.636	-0.614	-0.592
Linear Fit κ, Average α	R^2	0.99572	0.99750	0.99537	0.99616
	$\lVert\mathrm{Error}\rVert_2$	0.14572	0.13212	0.20101	0.20861
	κ	0.515	0.555	0.595	0.635
	α	-0.625	-0.625	-0.625	-0.625
Linear Fit κ & α (No $M_j = 1.35$)	R^2	0.99685	0.99755	0.99606	0.99718
	$\lVert\mathrm{Error}\rVert_2$	0.12486	0.13087	0.18548	0.17868
	κ	0.529	0.566	0.602	0.639
	α	-0.599	-0.591	-0.5843	-0.577
Best κ, $\alpha = 0$	R^2	0.98464	0.98217	0.98344	0.98476
	$\lVert\mathrm{Error}\rVert_2$	0.27591	0.35277	0.38014	0.41547
	κ	0.761	0.815	0.854	0.910
	α	0	0	0	0
Linear Fit κ, $\alpha = 0$	R^2	0.98463	0.98205	0.98329	0.98474
	$\lVert\mathrm{Error}\rVert_2$	0.27601	0.35400	0.38188	0.41574
	κ	0.763	0.811	0.859	0.908
	α	0	0	0	0
Alternate Method – Best Coefficients	R^2	0.99804	0.99739	0.99619	0.99832
	$\lVert\mathrm{Error}\rVert_2$	0.09846	0.13501	0.18223	0.13781
	κ	0.990	1.050	1.140	1.170
	α	0.180	0.150	0.210	0.170
Alternate Method – Linear Fit κ, Average α	R^2	0.99747	0.99840	0.99633	0.99775
	$\lVert\mathrm{Error}\rVert_2$	0.11202	0.10580	0.17906	0.15963
	κ	0.993	1.056	1.119	1.182
	α	0.178	0.178	0.178	0.178
Alternate Method – Best κ, $\alpha = 0$	R^2	0.99417	0.99723	0.99397	0.99468
	$\lVert\mathrm{Error}\rVert_2$	0.16997	0.13903	0.22939	0.24552
	κ	0.870	0.940	0.980	1.040
	α	0	0	0	0

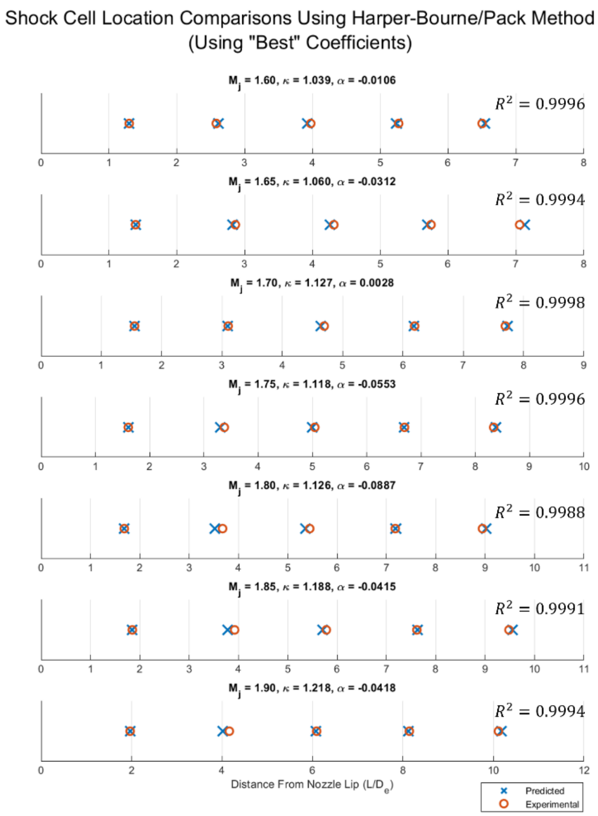

Figure B.1: Underexpanded shock location predictions using best coefficients

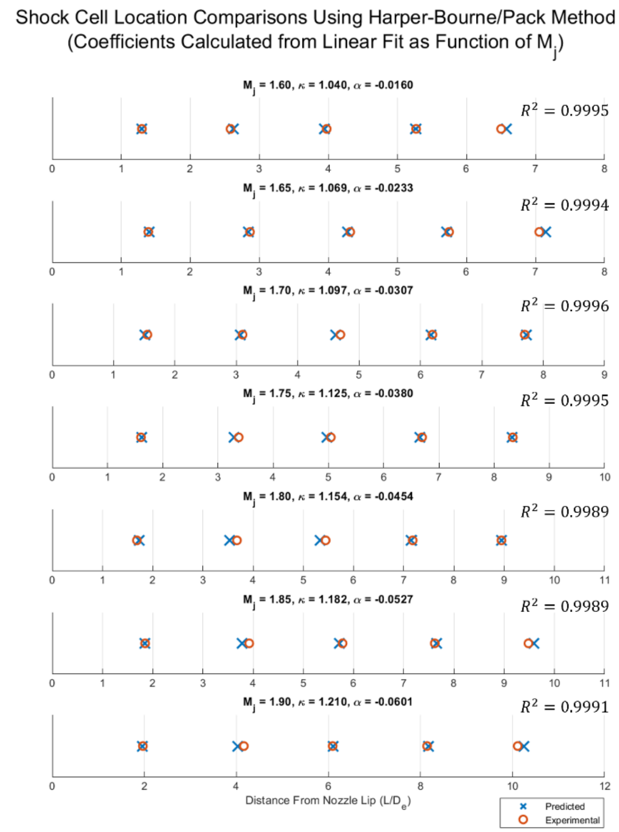

Figure B.2: Underexpanded shock location predictions using linear fit with M_j

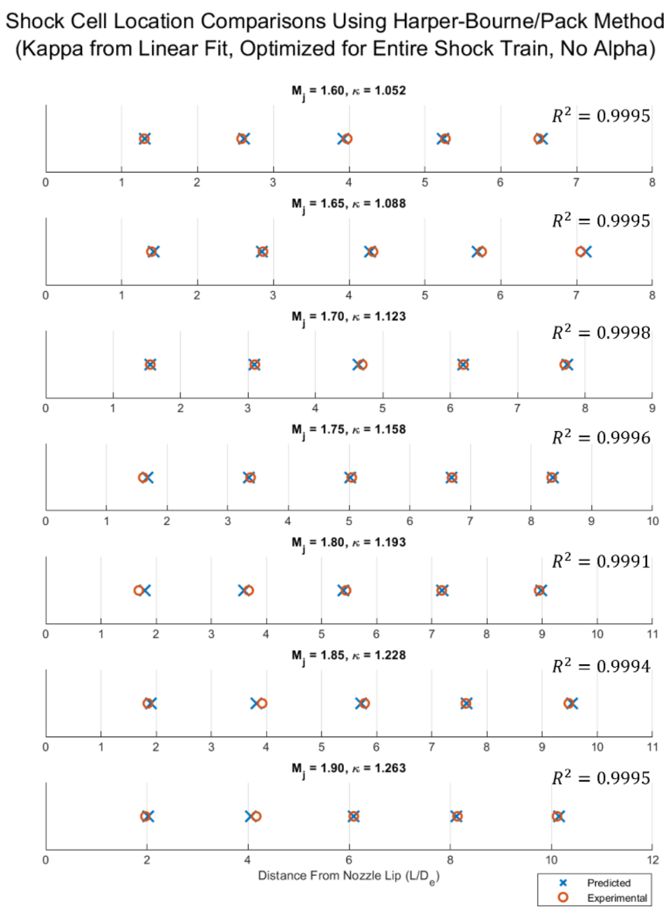

Figure B.3: Underexpanded shock location predictions using κ from linear fit and $\alpha = 0$

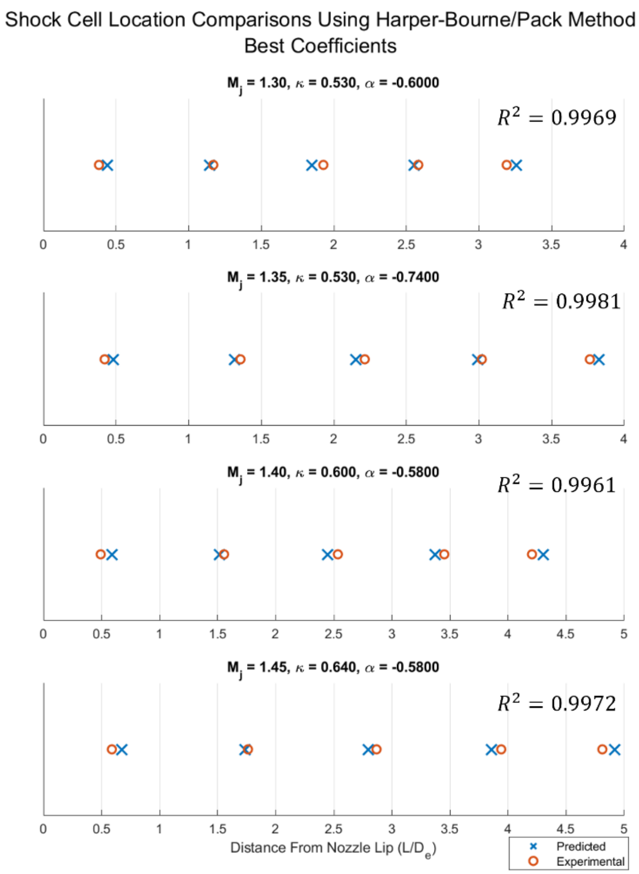

Figure B.4: Overexpanded shock location predictions using best coefficients

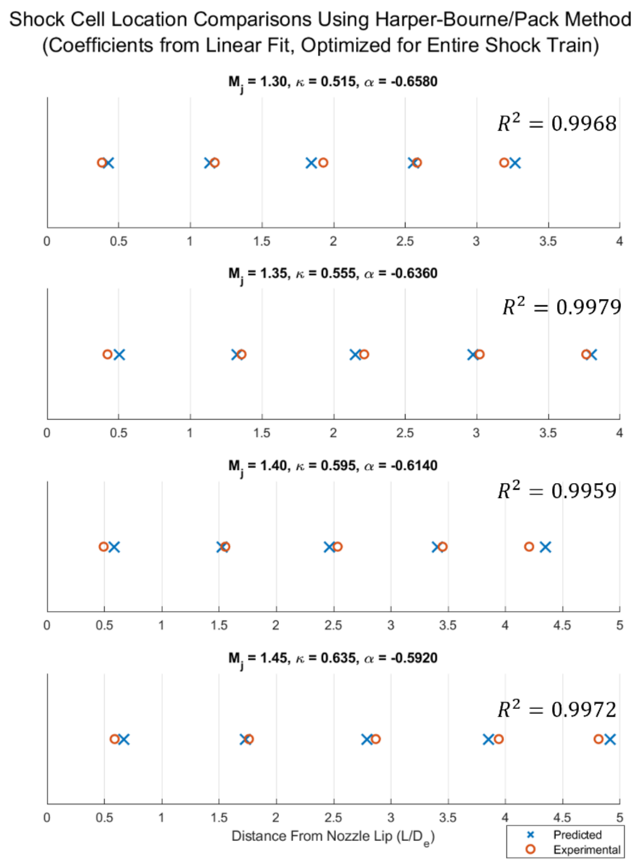

Figure B.5: Overexpanded shock location predictions using coefficients from linear fit

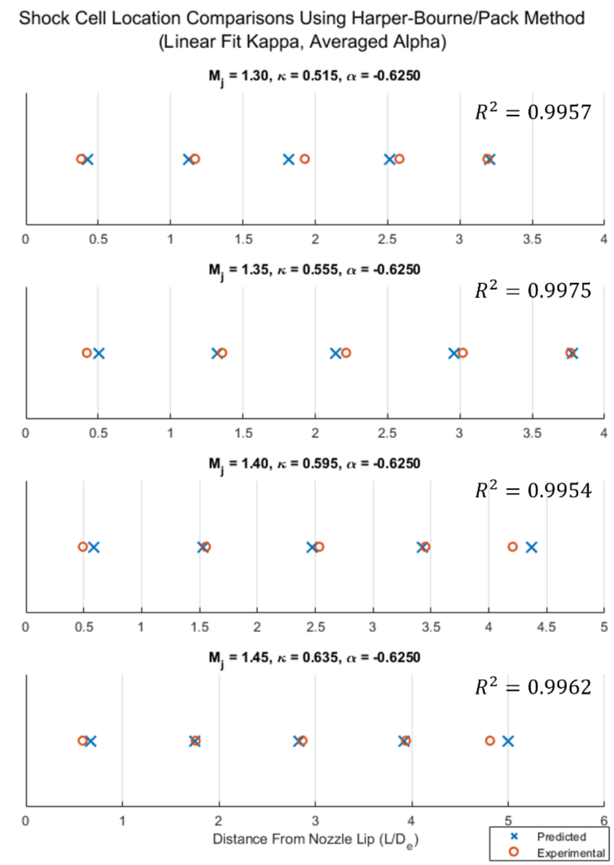

Figure B.6: Overexpanded shock location predictions linear fit κ and averaged α

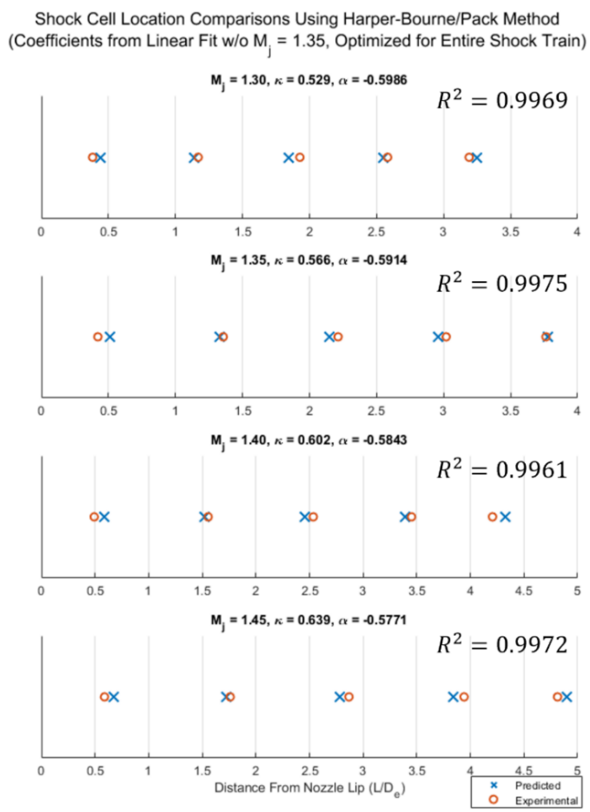

Figure B.7: Overexpanded shock location predictions using coefficients from linear fit (excluding $M_j = 1.35$)

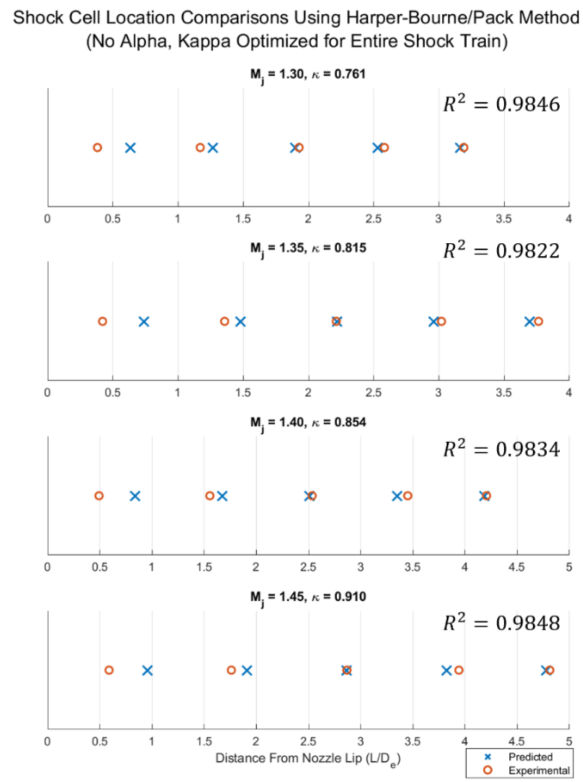

Figure B.8: Overexpanded shock location predictions using best κ values and $\alpha = 0$

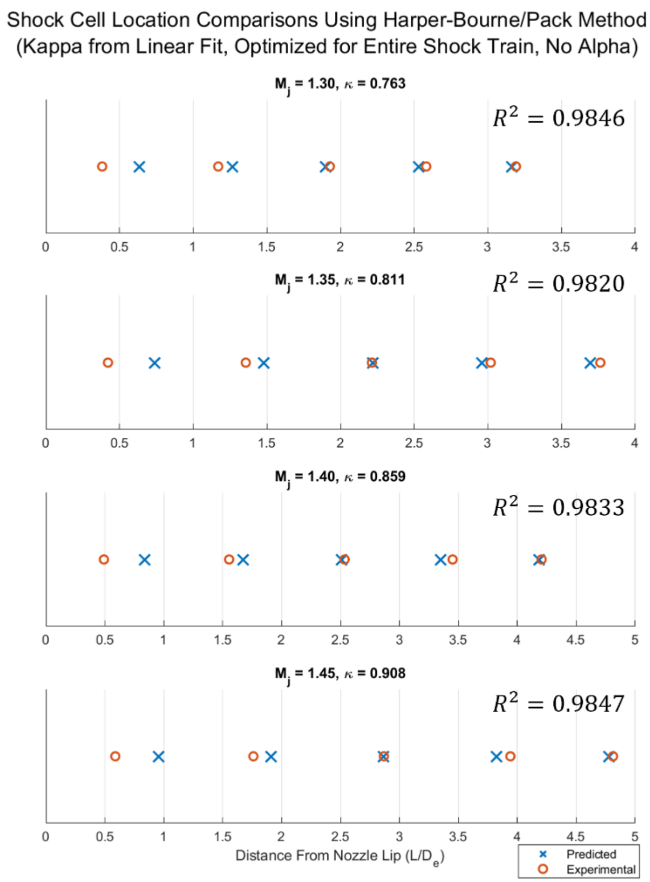

Figure B.9: Overexpanded shock location predictions using κ from a linear fit and $\alpha = 0$

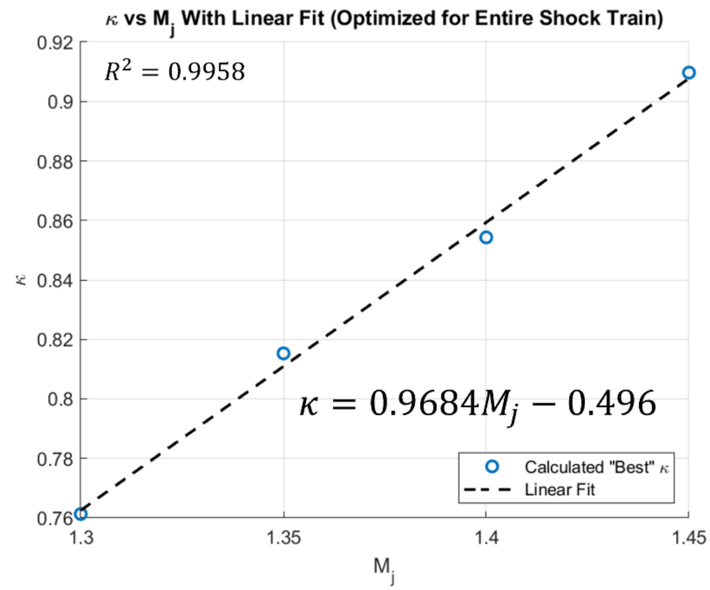

Figure B.10: Linear fit of κ with M_j for best kappa at $\alpha = 0$

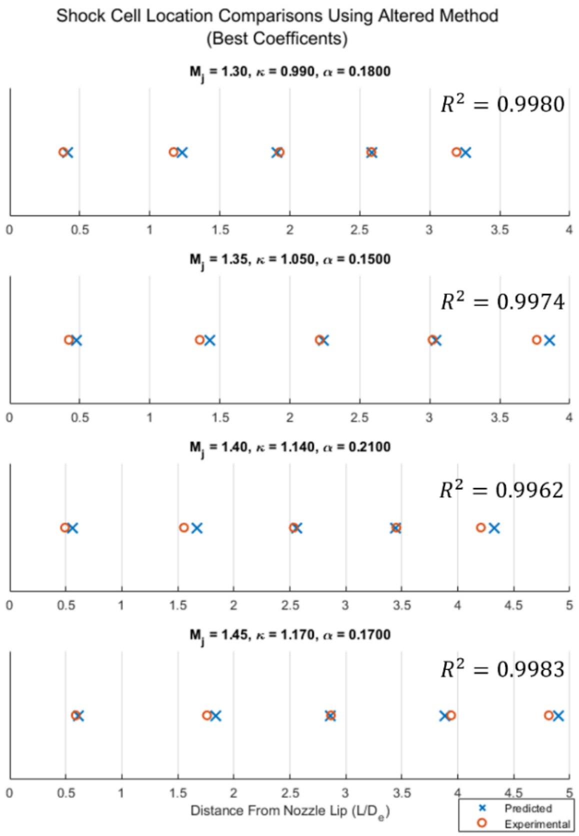

Figure B.11: Overexpanded shock location predictions using altered method and best coefficients

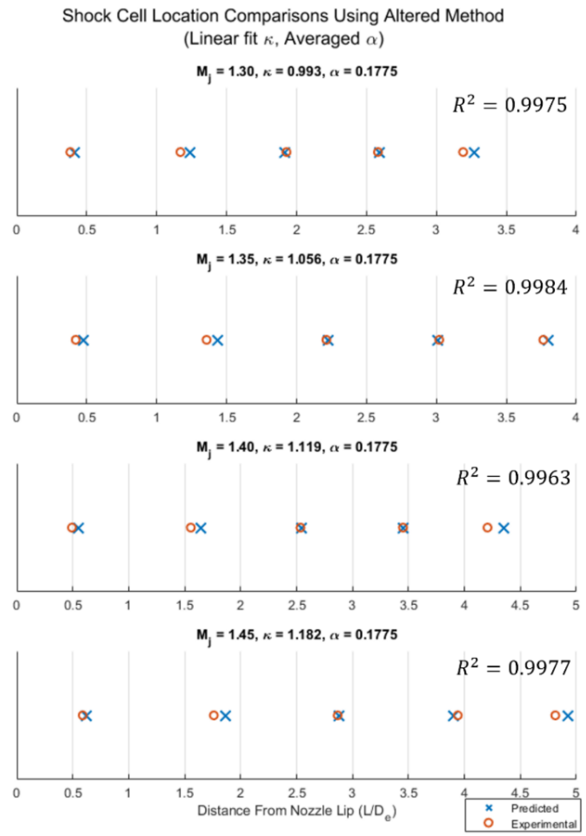

Figure B.12: Overexpanded shock location predictions using altered method with linear fit κ and averaged α

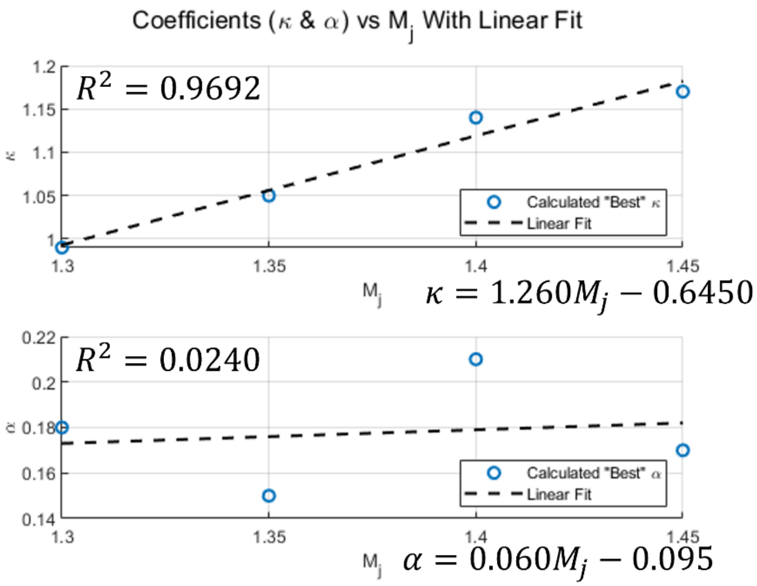

Figure B.13: Linear fit coefficients for overexpanded regime using altered method

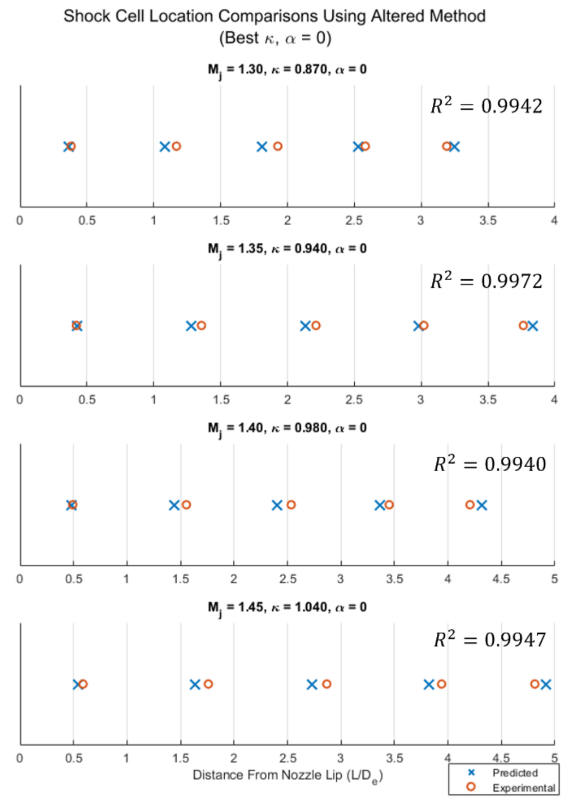

Figure B.14: Overexpanded shock location predictions using altered method with best κ values and $\alpha = 0$